

## Topological approach to void finding applied to the SDSS galaxy map

MANU AGGARWAL,<sup>1</sup> MOTONARI TONEGAWA,<sup>2</sup> STEPHEN APPLEBY,<sup>2,3</sup> CHANGBOM PARK,<sup>4</sup> AND VIPUL PERIWAL<sup>1</sup>

<sup>1</sup>*Laboratory of Biological Modeling/NIDDK, National Institutes of Health, Bethesda, Maryland, United States of America*

<sup>2</sup>*Asia Pacific Center for Theoretical Physics, Pohang, 37673, Korea*

<sup>3</sup>*Department of Physics, POSTECH, Pohang, 37673, Korea*

<sup>4</sup>*School of Physics, Korea Institute for Advanced Study, 85 Hoegiro, Dongdaemun-gu, Seoul, 02455, Korea*

### ABSTRACT

The structure of the low redshift Universe is dominated by a multi-scale void distribution delineated by filaments and walls of galaxies. The characteristics of voids; such as morphology, average density profile, and correlation function, can be used as cosmological probes. However, their physical properties are difficult to infer due to shot noise and the general lack of tracer particles used to define them. In this work, we construct a robust, topology-based void finding algorithm that utilizes Persistent Homology (PH) to detect persistent features in the data. We apply this approach to a volume limited sub-sample of galaxies in the SDSS I/II Main Galaxy catalog with the  $r$ -band absolute magnitude brighter than  $M_r = -20.19$ , and a set of mock catalogs constructed using the Horizon Run 4 cosmological  $N$ -body simulation. We measure the size distribution of voids, their averaged radial profile, sphericity, and the centroid nearest neighbor separation, using conservative values for the threshold and persistence. We find 32 topologically robust voids in the SDSS data over the redshift range  $0.02 \leq z \leq 0.116$ , with effective radii in the range  $21 - 56 h^{-1}$  Mpc. The median nearest neighbor void separation is found to be  $\sim 57 h^{-1}$  Mpc, and the median radial void profile is consistent with the expected shape from the mock data.

### 1. INTRODUCTION

The cosmic web, as traced by galaxies in the late Universe, is an interesting feature of the gravitational collapse of an initially Gaussian density field that naturally appears and evolves in the late-time universe (Gregory & Thompson 1978; Jöeveer et al. 1978; Klypin & Shandarin 1983; White et al. 1987; Gott et al. 1986; Vogeley et al. 1994b; Bond et al. 1996; Colberg et al. 2005; Weygaert & Bond 2008; Codis et al. 2018; Libeskind et al. 2018; Park et al. 2022). In three dimensions, matter collapses locally in an anisotropic manner, from underdensities onto two-dimensional sheets, then into one-dimensional filaments and finally accreting into knots. Gravitational outfall from underdense regions generates large voids in the late Universe, bounded by the two-dimensional walls generated as a result of anisotropic collapse. Voids comprise the overwhelming majority of the spatial volume at  $z \simeq 0$  (Pan et al. 2012).

The defining characteristic of a void is a dearth of matter, which makes it difficult to quantify and measure. We observe galaxies, which comprise a relatively sparse point distribution that is biased relative to the dark matter field. Regions of space which are not well sampled will be heavily affected by noise when attempting to infer properties of the underlying matter density field. In spite of these difficulties, voids have proved to be a valuable source of cosmological information, and they have been applied to the Alcock-Paczynski test (Ryden 1995; Lavaux & Wandelt 2012; Sutter et al. 2012, 2014), and other forms of cosmological parameter estimation (Hamaus et al. 2015, 2020; Schuster et al. 2023; Contarini et al. 2022a,b; Kovács et al. 2022). Voids can also be used to test extensions to the standard model (Lee & Park 2009; Platen et al. 2008; Bos et al. 2012; Spolyar et al. 2013; Cai et al. 2015; Achitouv 2016; Woodfinden et al. 2022; Pollina et al. 2019; Verza et al. 2019; Massara et al. 2015; Chan et al. 2019; Nadathur et al. 2020).

manu.aggarwal@nih.gov

motonari.tonegawa@apctp.org

stephen.appleby@apctp.org

cbp@kias.re.kr

vipulp@nidk.nih.gov

To extract cosmological information from the distribution of voids, we must first measure their individual properties such as volume and morphology. Numerous different void finders are employed within cosmology for this purpose (Vogeley et al. 1994a; El-Ad & Piran 1997; Platen et al. 2007; Neyrinck 2008; Aragon-Calvo et al. 2010; Pan et al. 2012; Sutter et al. 2015). They typically involve searching for underdense regions with a fixed shape template (spherical, ellipsoidal), or generating a set of polygons from galaxy positions, assigning a local density to these shapes according to their volume and finally linking adjacent, low-density polygons to generate macroscopic structures (but see Shim et al. (2021b) and Shim et al. (2023) for a void definition not assuming any geometry). They yield somewhat different morphologies, density profiles etc, leading to some ambiguity in void properties. These different approaches are typically based on geometric assumptions and are fundamentally different from the mathematically rigorous topology computed by Persistent Homology (PH). The method of PH applies techniques developed in algebraic topology to find robust lacunae in noisy, discrete data sets. PH makes no assumptions about the geometry of voids *a priori*, which is important since the real universe consists of regions of relatively low density that are more often polyhedral than spherical (Neyrinck 2008; Icke & Weygaert 1987). Indeed, we do not expect voids to be spherical because the critical points of the Gaussian initial density field are generically ellipsoidal (Bardeen et al. 1986). As underdense regions grow in volume due to gravitational collapse onto surrounding walls, they have a tendency to become increasingly spherical. However, at late times they merge to form complex morphological structures (Sheth & van de Weygaert 2004; Jennings et al. 2013).

In this work, we apply the PH methodology to the SDSS main galaxy sample, inferring a number of key properties of voids in the low redshift universe; their size distribution, averaged radial profiles, sphericity, and the pairwise distribution of void voxels. We perform a comparative study between the data and mock galaxy catalogs and between our approach and another void finder in the literature.

The paper proceeds as follows. In Section 2 we provide a brief and non-technical review of some of the important aspects of the topological methodology employed in this work. In Section 3 we introduce the galaxy catalog from which voids are extracted and the mock data that is used for comparative purposes. Section 4 contains the main results of our analysis; the properties of voids found using PH in the data and mock catalogs. We compare our results with other void finders in the literature in Section 4.2, and discuss our findings in Section 5. The appendix contains some of the more technical details of the numerical algorithms used in the main body of the paper.

## 2. INTRODUCTION TO PERSISTENT HOMOLOGY

We begin with a brief review of some of the important underlying ideas used in topological data analysis, in particular for the void finding algorithm applied to galaxy data in Section 4. The discussion is intended to be non-technical; further details can be found in the appendices.

A homology group is a collection of sets of cycles such that any two cycles in the same set can be continuously deformed into one another and those in different sets cannot. For example, all cycles on the surface of a sphere can be shrunk or contracted continuously along its surface to a point (see Figure 1A top panel). On the other hand, Figure 1 also shows three homologically distinct cycles on the surface of a 2-torus (Figure 1A bottom panel). Cycle  $c$  can contract to a point, whereas cycles  $a$  and  $b$  can neither contract to a point nor can be deformed to each other. We say that cycle  $c$  is contractible (belonging to the trivial homology), and  $a$  and  $b$  are non-contractible cycles in different equivalence classes of the homology group of dimension one ( $H_1$ ). Moreover, any non-contractible cycle on the surface of a torus can be deformed either to  $a$  or to  $b$ . Hence, there are exactly two topologically distinct holes in this shape, and  $a$  and  $b$  are examples of representative boundaries for these. This gives a classification of the shape of the surface of a 2-torus based on the number of homologically distinct non-contractible cycles on its surface. In this example, we discussed cycles on the surface of the torus which are also called cycles of dimension one and belong to the homology group of dimension one. Similarly, the homology group of dimension two ( $H_2$ ) is the collection of sets of non-contractible cycles of dimension two. Intuitively, they can be thought of as non-contractible surfaces around voids in a point-cloud (i.e., a discrete set of points) embedded in a three-dimensional Euclidean space.

In real-life applications, experimental data are often discrete observations that can be embedded as a point-cloud and not a smooth manifold. Homology groups of a point-cloud can be computed by constructing simplices. Briefly, a  $n$ -simplex is a set of  $n+1$  points. For example, 0-simplices are points, 1-simplices are edges, 2-simplices are triangles, and 3-simplices are tetrahedrons. A collection of simplices is called a simplicial complex. Figure 1B shows two simplicial complexes. Complex  $K_1$  has a hole of dimension 1 and the edges in the simplex form a representative boundary around this hole. The complex  $K_2$  contains triangles  $\{a, b, c\}$  and  $\{a, c, d\}$  along with the simplices of  $K_1$ . Visually, these are

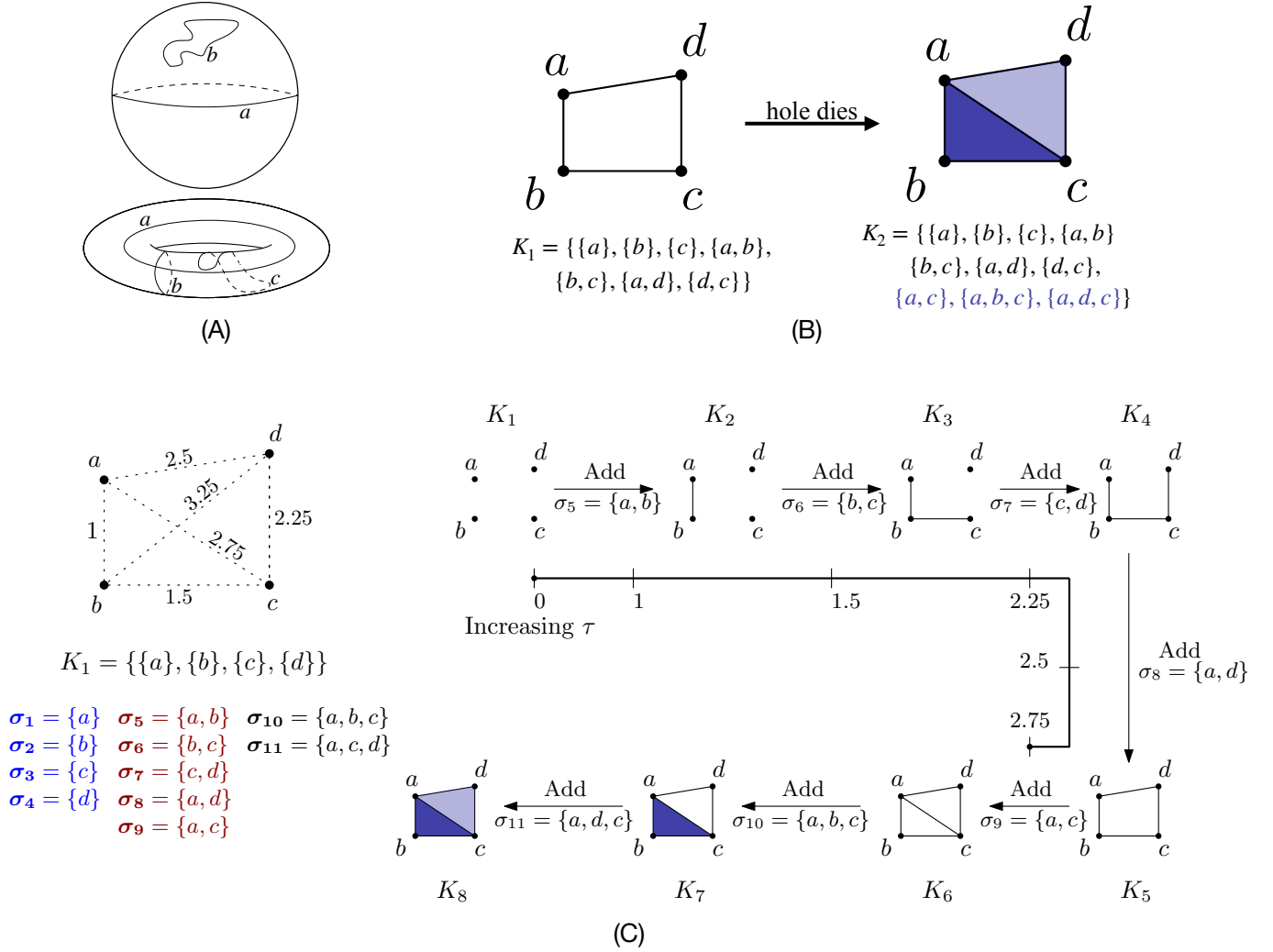


**Figure 1.** (A) Top panel shows two cycles  $a$  and  $b$  on the surface of a sphere. Both can be continuously deformed along the surface of the sphere to the same point. Any cycle on the surface of a sphere can contract to a point. Bottom panel shows three cycles on the surface of a 2-torus. Cycle  $c$  contracts to a point. Cycles  $a$  and  $b$  are non-contractible and cannot be deformed to each other. Any non-contractible cycle on the surface of the torus can deform to either  $a$  or to  $b$ . (B) A hole dies when its triangulation gets filled-in. The hole in simplicial complex  $K_1$  dies when edge  $\{a, c\}$  and triangles  $\{a, b, c\}$  and  $\{a, d, c\}$  are added to it to give new complex  $K_2$ . (C) (from Aggarwal & Periwai (2023)) Vietoris-Rips filtration on a discrete set of points. The simplicial complex at a given value of  $\tau$  is a collection of all simplices with diameter at most  $\tau$ . Number of holes is initially 0. One hole is born at spatial scale of  $\tau = 2.5$  when edge  $\{a, d\}$  is added. Another is born when  $\{a, c\}$  is added at  $\tau = 2.75$ . Both holes get filled in, or die, at  $\tau = 2.75$  when triangles (2-simplices) are added to the simplicial complex. The first hole has persistence  $2.75 - 2.5 = 0.25$ . The second hole dies at the same spatial scale it is born and so has persistence 0.

shown as the two filled-in triangles in  $K_2$  in the figure. Naively, we can note that the hole in  $K_1$  is filled in when its triangulation is added to the complex. We say that the hole in  $K_1$  dies when the triangles  $\{a, b, c\}$  and  $\{a, c, d\}$  are added to it. Simplicial homology rigorously defines this notion of holes and their birth and death using algebraic topology, and it generalizes to high dimensions. Readers interested in the mathematical and computational details are directed to Edelsbrunner & Harer (2022).

When a discrete set is embedded in a Euclidean space, we can compute its homology groups at different spatial scales. Vietoris-Rips filtration (VR-filtration) is a commonly used construction of simplicial complexes at different spatial scales. The simplicial complex at spatial scale  $\tau$  is defined as the collection of all simplices that have  $\tau$  as the maximal pairwise distance between their points. As the spatial scale changes, the simplicial complex changes, and

there might be birth and death of holes (Figure 1C). PH computes these births and deaths, and they are plotted as persistence diagrams (PD).

They give a global multi-scale overview of the topology of the shape of the discrete data set. Persistence of a topological feature, or a hole, is defined as the duration  $\tau$  between its death and birth. Features with a large persistence are usually deemed as topologically significant. Due to its generality and computation of robust topological features in noisy data sets across multiple scales, PH has found useful applications in areas as diverse as neuroscience (Bendich et al. 2016), computational biology (McGuirl et al. 2020), natural language processing (Zhu 2013), the spread of contagions (Taylor et al. 2015), cancer diagnosis (Nicolau et al. 2011; Lawson et al. 2019), material science (Kramár et al. 2013), computer graphics (Brüel-Gabrielsson et al. 2018), cosmology (Melott 1990; Mecke et al. 1994; Kerscher et al. 1998; Sousbie et al. 2011; Park et al. 2013; Pranav et al. 2019; Feldbrugge et al. 2019; Wilding et al. 2021; Pranav 2021) among many others. In the context of cosmology, homology groups are associated with different cosmic environment types as follows. Connected components (0-dimensional homology groups,  $H_0$ ), loops (1-dimensional homology groups,  $H_1$ ), and low-density 3D volumes (2-dimensional homology groups,  $H_2$ ) are analogous to galaxy clusters, closed loops of filaments, and cosmic voids, respectively (Xu et al. 2019). Locations of voids can be estimated by computing representative boundaries of topologically significant  $H_2$  features. However, the representatives are not unique by definition (Carlsson 2009). We define tight representatives as those with shorter lengths (fewer number of simplices in the boundary). Computing optimal tight representatives is computationally intractable even for a few thousand points. Aggarwal & Periwai (2023) developed an algorithm for large data sets that computes representatives that may not be optimal but are significantly shortened as compared to those obtained from the matrix reduction algorithm by default. Using it, we find geometrically precise boundaries around significant topological features in the SDSS and HR4 data sets which have more than a hundred thousand galaxies.

### 3. DATA

#### 3.1. SDSS spectroscopic sample

To construct void catalogs we require a galaxy catalog, preferably with certain desirable properties. The data should be contiguous on the sky, have high angular completeness, and be volume limited. Three-dimensional void construction may be severely impaired by the presence of a significantly varying angular selection function on the sky, and similarly by systematic variation in the number density with redshift. We also require a point distribution that occupies a large volume, to generate a statistical sample that can be useful for cosmology and also to capture the morphology of the largest voids. Given these requirements, the SDSS I+II DR7 Main Galaxy catalog is ideally suited for our purpose. Specifically, we adopt the Korea Institute for Advanced Study Value Added Galaxy Catalog (KIAS-VAGC; Choi et al. 2010), which is based on the original catalog (Blanton et al. 2005) but is supplemented with additional redshift information from the Zwicky catalog (Falco et al. 1999), the IRAS Point Source Catalog Redshift Survey (Saunders et al. 2000), the Third Reference Catalog of Bright Galaxies (de Vaucouleurs et al. 1991) and the Two-Degree Field Galaxy Redshift Survey (Colless et al. 2001), together with the updated angular selection function.

The catalog contains 593,514 redshifts, with  $r$ -band Petrosian magnitudes in the range  $10 < r_p < 17.6$ . Since we require contiguous data, we remove the three southern stripes and the Hubble Deep Field region. Approximately 90% of the angular mask has completeness higher than 95%. In Figure 2 (right panel) we present the completeness of the angular selection function as a fraction of the area occupied on the sky. We also present the full galaxy catalog in angular coordinates (right ascension vs declination, left panel). The redshift and corresponding  $r$ -band absolute magnitude cuts are  $0.02 \leq z \leq 0.116$  and  $M_r \leq -20.19$  respectively<sup>1</sup> for the volume limited subsample that we select for our analysis. The evolution correction for the absolute magnitudes,  $E(z) = 1.6(z - 1)$ , is applied (Tegmark et al. 2004). In the middle panel of Figure 2, we present the number density of this volume limited sample as a function of comoving distance, assuming a flat  $\Lambda$ CDM cosmology with  $\Omega_m = 0.3$ . The black solid line is the number density of the SDSS data, and the blue points/errorbars are the mean and rms of the mocks, described in the following section.

For the purposes of our study, the SDSS galaxies are not weighted by the angular selection function at any point during the persistent homology calculation and subsequent void finding algorithm. Because the completeness of the value added catalog is so high in this particular data set, we do not expect the angular selection function to have any significant effect on the resulting properties of the voids. This may be an issue for higher redshift data, where the completeness on the sky is generally lower and data quality is worse.

<sup>1</sup> The term  $+5 \log h$  is dropped, i.e.,  $h = 1$  is used, in the conversion from apparent magnitudes to absolute magnitudes.

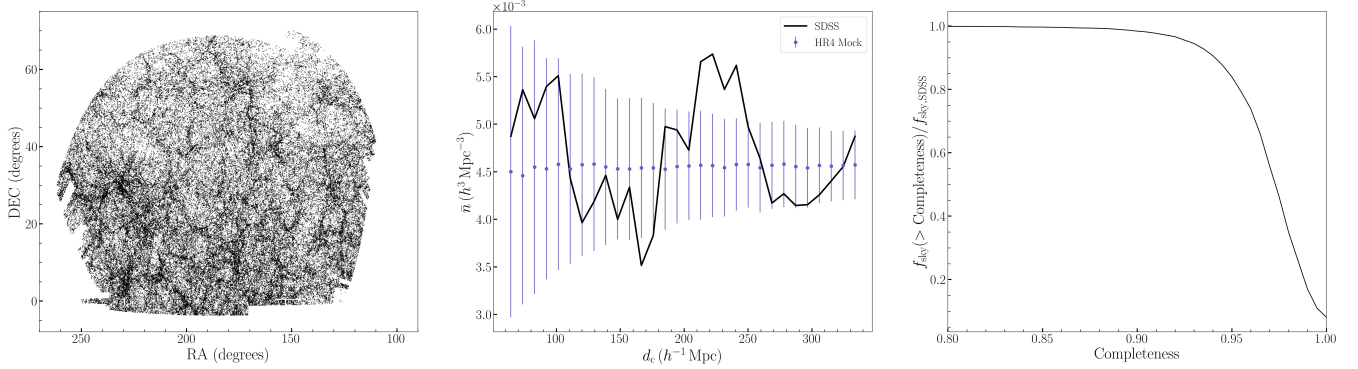


**Figure 2.** The SDSS galaxy point distribution as a function of angular coordinates on the sky (left panel). The number density  $\bar{n}$  of the SDSS volume limited sample as a function of comoving distance is presented in the middle panel (solid black line), along with the mean and RMS values of the mocks (blue points/errorbars). In the right panel, we present the fraction of the SDSS footprint as a function of its angular completeness. approximately 90% of the footprint has completeness greater than 0.95.

### 3.2. Mock Galaxy Data

We compare the void catalog from the SDSS data to mock catalogs designed to match the clustering properties of the observed galaxy distribution. For this purpose, we adopt the Horizon Run 4 (HR4) simulation. HR4 is a cosmological scale  $N$ -body simulation in which  $6300^3$  cold dark matter particles were gravitationally evolved in a  $V = (3150 h^{-1} \text{Mpc})^3$  box using a modified version of GOTPM code<sup>2</sup>. The WMAP5 cosmology (Komatsu et al. 2009) is used for this simulation. Details of the simulation can be found in Kim et al. (2015). Dark matter halos and subsequently mock galaxy catalogs are constructed in Hong et al. (2016) using a most-bound halo particle-galaxy correspondence algorithm, with satellite galaxy survival time after mergers calculated using a modified model of Jiang et al. (2008)

$$\frac{t_{\text{merge}}}{t_{\text{dyn}}} = \frac{(0.94\epsilon^{0.6} + 0.6) / 0.86}{\ln [1 + (M_{\text{host}}/M_{\text{sat}})]} \left( \frac{M_{\text{host}}}{M_{\text{sat}}} \right)^{1.5}, \quad (1)$$

where  $t_{\text{dyn}}$  is a dynamical timescale – the orbital period of a virialized object –  $M_{\text{host}}, M_{\text{sat}}$  are the host halo and satellite masses, and  $\epsilon$  is the circularity of the satellite’s orbit at the time of merger. The particle and halo mass resolutions of the simulation are  $9.0 \times 10^9 h^{-1} M_{\odot}$  and  $2.7 \times 10^{11} h^{-1} M_{\odot}$ , respectively.

We use the  $z = 0$  snapshot box to generate mock catalogs –  $N_r = 360$  observers are placed in the box, maximally separated to ensure the mock data does not overlap. To reproduce the survey geometry of the SDSS data we use, the SDSS angular footprint is applied relative to each observer placed at the corners. A global mass cut is applied to all galaxies in the snapshot box to ensure that the average number density  $\bar{n}$  matches that of the SDSS data,  $\bar{n} = 4.6 \times 10^{-3} (h^3 \text{Mpc}^{-3})$ . For absolute magnitude-limited catalogs with a high magnitude selection function like the one used in this work, simulated data with a mass cut typically provides a very good match to a magnitude cut.

The galaxy positions that we obtain from spectroscopic redshifts are shifted by Doppler effect due to the radial component of their own motions. This effect is called the redshift space distortions (Kaiser 1987), and the modulation from the real-space position  $\mathbf{r}$  to the redshift-space (observed) position  $\mathbf{s}$  caused by the galaxy velocity  $\mathbf{v}$  is expressed as

$$\mathbf{s} = \mathbf{r} + \frac{1}{aH} \hat{\mathbf{e}}_{\parallel} (\mathbf{v} \cdot \hat{\mathbf{e}}_{\parallel}), \quad (2)$$

where  $a$ ,  $H$ , and  $\hat{\mathbf{e}}_{\parallel}$  are the scale factor, Hubble parameter, and the unit vector along the joining line between a galaxy and the observer. We apply this correction to each simulated galaxy to generate the redshift-space mock catalogs that are consistent with the observation data. We only perform the PH analysis for the redshift-space mocks and do not repeat it for the real space as the purpose of mocks is to check the consistency between observational data and the

<sup>2</sup> The original GOTPM code is introduced in Dubinski et al. (2004). A review of the modifications introduced in the Horizon Run project can be found at <https://astro.kias.re.kr/~kjhan/GOTPM/index.html>

predictions from the  $\Lambda$ CDM cosmology simulation. Studying the difference in void statistics for these two spaces is beyond the scope of the present study and will be pursued in future works.

## 4. RESULTS

### 4.1. Topologically significant voids computed for SDSS DR7 and mocks exhibit similar properties

We compute PH of SDSS DR7 for Vietoris-Rips filtration (VR-filtration, see Appendix A) up to a threshold for the spatial scale of  $36 h^{-1}$  Mpc. Figure 3A shows the resulting  $H_2$  PD, and in particular presents an important characteristic of the cosmic web – it is a multi-scale phenomenon. Voids are born, die and exhibit persistence thresholds over the entire range of scales that can be reasonably probed by the SDSS data, from  $1 h^{-1}$  Mpc to  $50 h^{-1}$  Mpc. We define a feature to be significant if it has persistence at least  $7.5 h^{-1}$  Mpc (persistence threshold) and is born before  $22.5 h^{-1}$  Mpc (birth threshold). We explain these choices in detail in Appendix D. Subsequently, there are 57 significant topological features in SDSS. Based on our choice of thresholds, it suffices to compute PH up to  $30 h^{-1}$  Mpc to determine the significant features in all of the mocks. This reduces computational run time by more than a factor of three as compared to the computation up to  $36 h^{-1}$  Mpc. Computation costs for computing PH up to  $30 h^{-1}$  Mpc and representative boundaries of non-trivial features are shown in Appendix G.1. With our choice, we are selecting objects that are present at scales  $\gtrsim \mathcal{O}(10 h^{-1} \text{Mpc})$ , which are those typically parsed by the cosmology community.

Figure 3B shows a kernel density estimation (KDE) plot of distributions of births and deaths of significant features in all mocks, along with those in SDSS (white x markers). The overlay shows that  $H_2$  topology is similar across mocks and SDSS. Figure 3C shows that the number of significant features in SDSS agrees with the median of the number of significant features in mocks. A total of 32 tight representatives around single significant voids were computed for SDSS. The number of tight representative boundaries is less than that of significant features due to generally larger birth scales and unchanged death scales after the shortening procedure. We explain this in Appendix C. Figure 3D shows the distribution of the number of tight representatives around single voids computed for mocks. Figure 3E shows three different views of all the representative boundaries computed in SDSS. We visually observe that the computed boundaries are polyhedral and not necessarily convex.

We compute the effective radius ( $R_{\text{eff}}$ ) of each void as the radius of the sphere with the same volume as the convex hull of its computed representative boundary. Cumulative probability density functions (CPDF) of  $R_{\text{eff}}$  distribution of all voids in SDSS is compared to that of mocks in Figure 4A. The distribution of  $R_{\text{eff}}$  of the voids computed for SDSS is compared to that of each of the 360 mocks using Mann-Whitney U test and Kolmogorov-Smirnov (KS) test. Figure 4B shows that the distribution of  $R_{\text{eff}}$  of the voids in the majority of the mocks is not significantly different from that of SDSS ( $p$ -value  $\gg 0.05$ ).

Figure 4C shows that the minimums of the effective radii computed for the mocks range from approximately 15 to  $30 h^{-1}$  Mpc and the medians range from 30 to  $40 h^{-1}$  Mpc, matching closely to SDSS. The maximums for the mocks, however, show a wider range of, approximately, 40 to  $80 h^{-1}$  Mpc.

Since computed  $H_2$  representatives are polyhedral that might be very different from spherical approximations of boundaries of voids, for additional validation we compute the radial distribution function  $g(r)$  for each void with the centroid of its computed representative boundary as the reference point. Briefly,  $g(r)$  is the ratio of density of shells of thickness  $2 h^{-1}$  Mpc around the centroid of the void to the density of shells containing a random point distribution ( $\approx 10^6$  points) distributed uniformly in the SDSS footprint. It is normalized by the mean value of the mocks at  $r = 4R_{\text{eff}}$ , and the radii of the shells are finally normalized by  $R_{\text{eff}}$ . Hence,  $g(r) > 1$  ( $g(r) < 1$ ) indicates overdense (underdense) regions. This ratio accounts for the fact that at large distances from the centroid location, the shells will hit the boundary of the survey. So, the density of the galaxies will artificially drop but so will the density of random points.

Figure 4D shows the  $g(r)$  profiles of each void in SDSS for which a representative boundary was computed using PH. On average,  $g(r)$  rises for  $r < R_{\text{eff}}$  with peak very close to  $r = R_{\text{eff}}$ . Figure 4E shows that the averages of  $g(r)$  profiles of all mocks present a similar profile to the average of the SDSS. We note that the peak is not exactly at  $r = R_{\text{eff}}$  presumably because the voids in the universe are not exactly spherical. We quantify this by computing sphericity ( $\psi$ ) as the ratio of  $4\pi R_{\text{eff}}^2$  to the surface area of the computed polyhedral boundary. Figure 4F shows that the sphericity of all voids is less than 1 but more than 0.6. The average sphericity of the voids is around 0.8 in every configuration (SDSS and the 360 mocks). The distribution of the sphericities of the voids in the 360 mocks is compared to the distribution of those in SDSS using the Mann-Whitney U test and the Kolmogorov-Smirnov (KS) test. Figure 4G shows that the majority of mocks do not show significant differences ( $p$ -value  $> 0.05$ ) in sphericities of the voids as compared to SDSS.

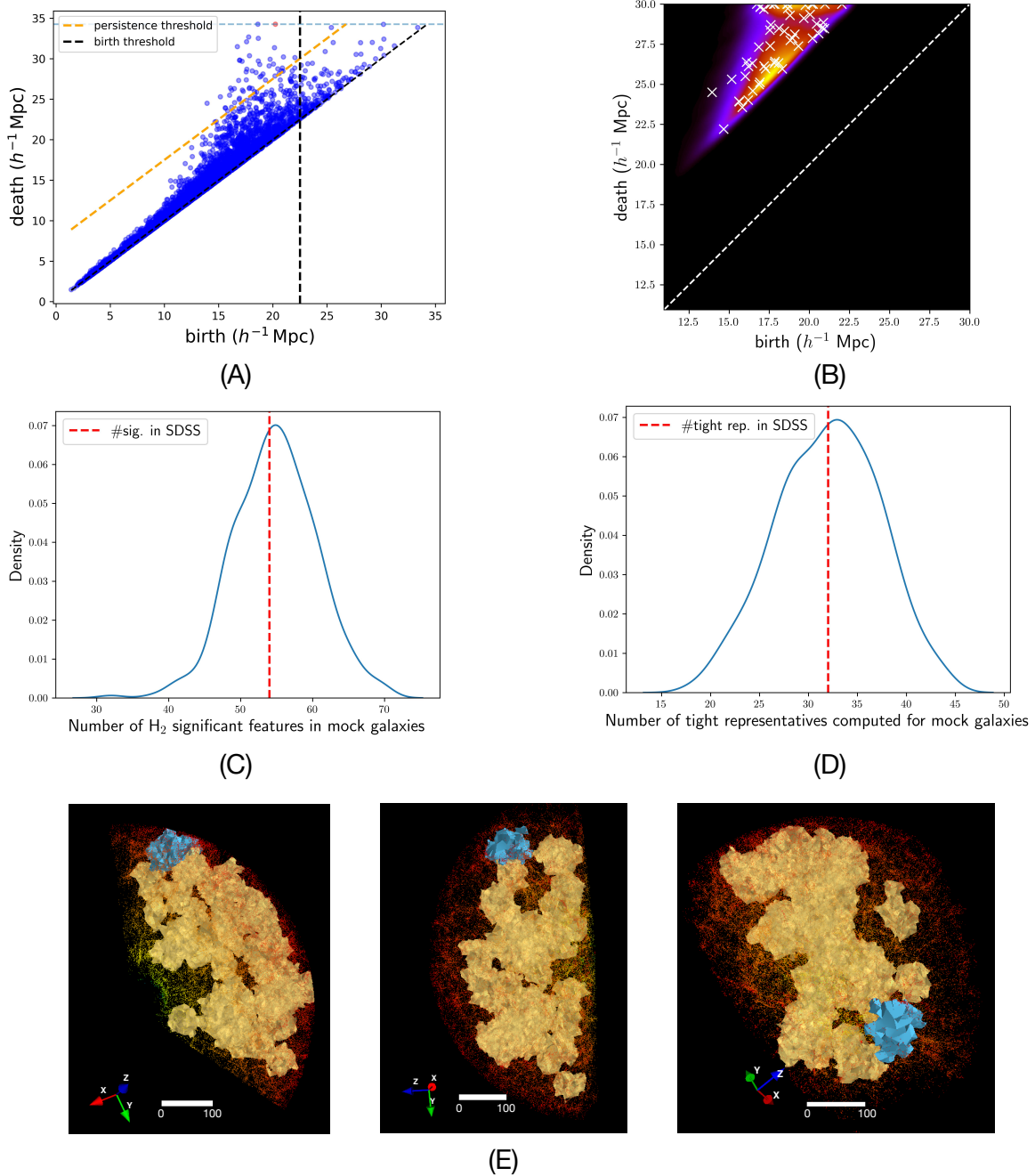


**Figure 3.** Topology of the mocks agrees with SDSS. (A)  $H_2$  PD for SDSS DR7 computed till a threshold of  $30 h^{-1}$  Mpc. Significant features are defined as those above the orange dashed line (persistence threshold of  $7.5 h^{-1}$  Mpc) and to the left of the black dashed line (birth threshold of  $22.5 h^{-1}$  Mpc). (B) KDE plot of significant features over all mocks. Significant features in SDSS are shown by white x markers. (C) Number of significant  $H_2$  features. (D) Distribution of numbers of computed tight  $H_2$  representatives in mocks. (E) Three views of computed tight  $H_2$  representatives in SDSS. One of the voids is highlighted in blue color.

We expect voids to be aspherical because of the complex morphological structure of the cosmic web, and also due to intrinsic anisotropic observational artifacts such as redshift space distortion and the Alcock-Paczynski effect.

Figures 5A and 5B show the PH voids computed in SDSS. For each void center, we compute the distance of the nearest void center from it. Figure 5C shows the two-point correlation function of void centers. We use the Landy-Szalay estimator (Landy & Szalay 1993),  $\xi(r) = \frac{DD-2DR+RR}{RR}$ , where  $DD$  takes the pair count of void centers in

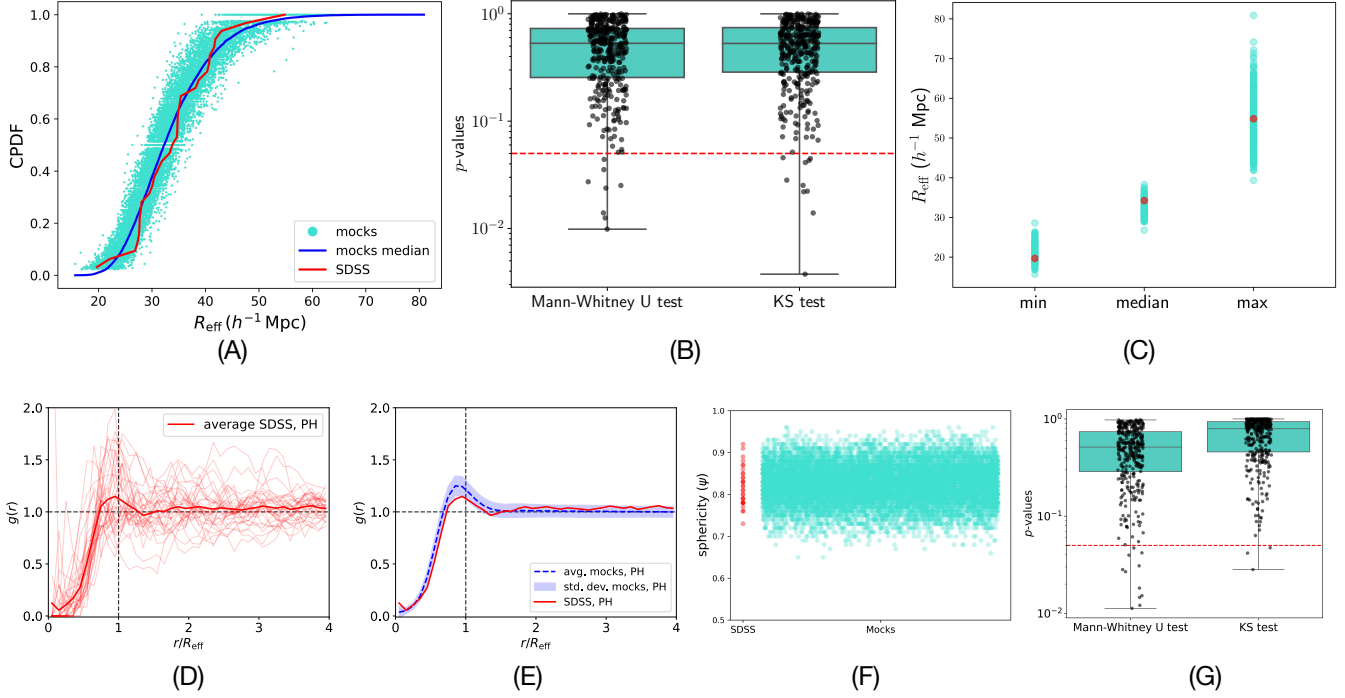


**Figure 4.** SDSS and the 360 mocks exhibit similar morphology. (A) Cumulative PDF (CPDF) of  $R_{\text{eff}}$  for SDSS (red) and all mocks (turquoise). (B)  $p$ -values from Mann-Whitney U and KS significance tests comparing the distribution of  $R_{\text{eff}}$  of voids in SDSS to the distributions of  $R_{\text{eff}}$  of voids in the mocks. Majority are greater than 0.05 (red dashed line). (C) Minimums, medians, and maximums of distributions of effective radii of voids computed for mocks (turquoise) and SDSS (red). (D) Radial distribution functions of each void that is computed for SDSS. The average of radial distributions over all voids is shown in a bold red line plot. (E) Averages of radial distribution functions of voids computed for mocks follow similar pattern to the average of the voids in SDSS. (F)  $p$ -values from Mann-Whitney U and KS significance tests show that the sphericities of voids is less than 1 but greater than 0.6. (G)  $p$ -values from comparing distributions of sphericities of voids in mocks to that in SDSS.

separation bins  $[r - \Delta r, r + \Delta r]$ ,  $RR$  is the pair count of random points distributed within the SDSS survey volume, and  $DR$  is the cross pair count between void centers and randoms. The number of random points is set to be sufficiently large, and  $DR$  and  $RR$  are normalized to  $DD$  accordingly. We observe that  $\xi(r)$  is peaked at  $\sim 50\text{--}60 h^{-1}\text{Mpc}$  and approaches zero as separation  $r$  increases. This means that the separation of voids is typically  $\sim 60 h^{-1}\text{Mpc}$ , which is also observed in Figure 5D. The drop below  $50 h^{-1}\text{Mpc}$  is due to the size of voids, i.e., the exclusion of other voids (Hamaus et al. 2014; Baldauf et al. 2016; Shim et al. 2021a). Figure 5D shows the distribution of nearest neighbor distances for the SDSS. The KDE of this distribution is shown in red; the majority of nearest void centers are within  $40$  to  $60 h^{-1}\text{Mpc}$ . Figure 5E shows KDEs of similar distributions for all of the mocks (turquoise). Although noisy due to a low number of objects in each realization, we find that the peak in the median of the KDEs of mocks (blue) matches with the peaks in the KDE of the SDSS (red).

The measured two-point statistics of the void centers – nearest neighbor separation and correlation function – present behaviour that is typical of critical points (Lumsden et al. 1989). The anti-clustering (‘exclusion’) regime of the correlation function  $r < 50 h^{-1}\text{Mpc}$  is related to our choice of birth and persistence thresholds because these indirectly determine the comoving size of the voids. In terms of critical points of some underlying continuous field traced by the galaxies, the exclusion zone can be understood as the typical length scale required for the curvature of the field to change signs twice between adjacent voids (Shim et al. 2021a).

#### 4.2. Comparison with Other SDSS Void Catalogs

Douglass et al. (2023) compute and compare void catalogs for SDSS DR7 using two popular classes of void finding algorithms, VoidFinder (El-Ad & Piran 1997) and  $V^2$  (Neyrinck 2008). The former computes voids by first expanding spheres centered at locally empty regions till they are bounded by a threshold number of galaxies, and these spheres are then merged to define voids (Douglass et al. 2023). The latter first computes a 3D Voronoi tessellation of the distribution of galaxies, then combines computed Voronoi cells into zones using watershed segmentation, which are



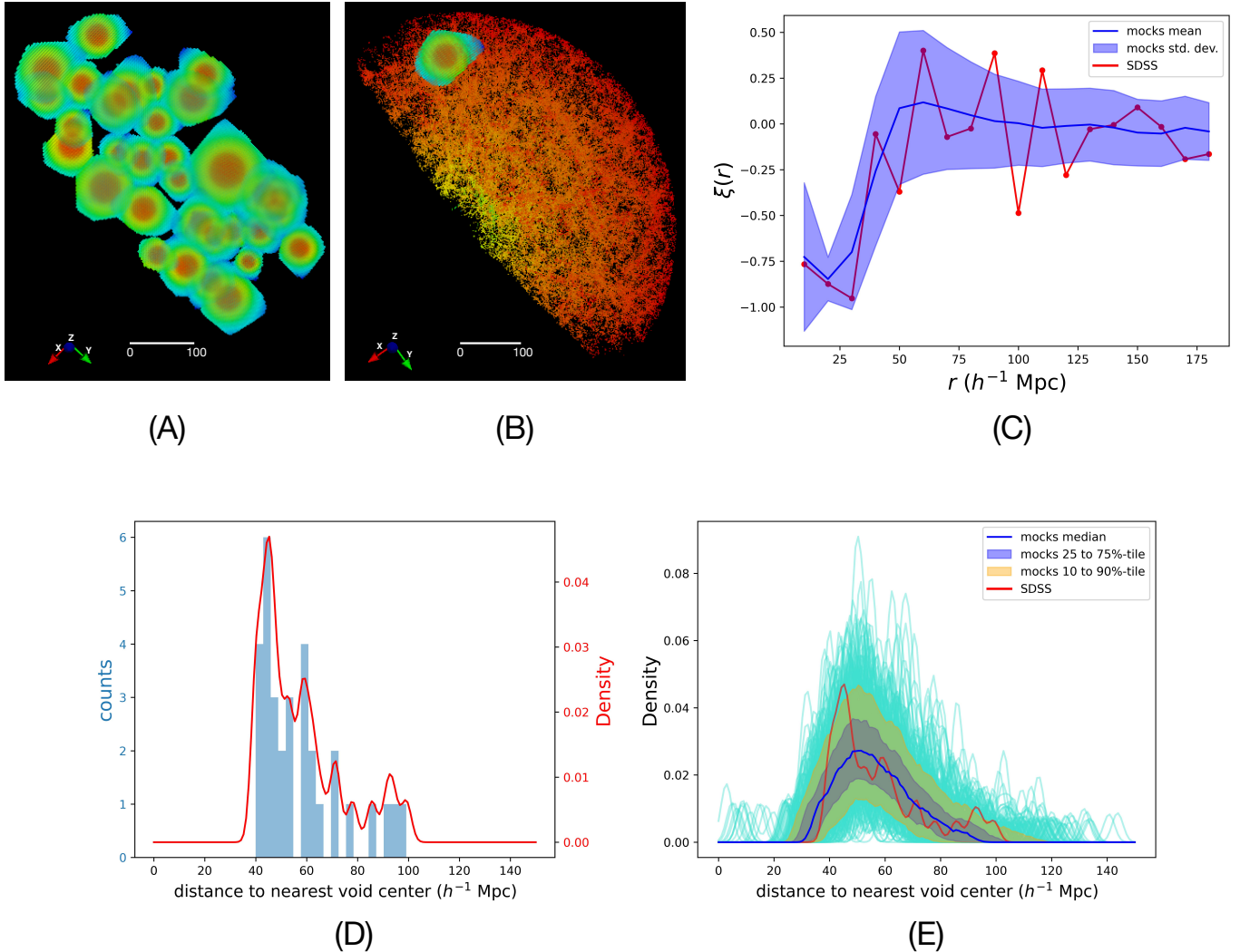


**Figure 5.** Characteristic distances between nearest void centers. (A) All cubic voxels that are inside voids computed for SDSS. (B) An example of cubic voxels inside one of the computed voids in SDSS. The color scheme is scaled based on the distance of voxels from the centroid of the void it is in. (C) The two-point correlation function of the void central positions. The red line represents the SDSS data, while the blue line and area indicate the mean and standard deviation from mocks. (D) Distribution of distances of the nearest void center to all void centers. The KDE of the distribution is shown in red. (E) KDE of the distributions of distances of the nearest void center to all void centers for the mocks (turquoise). The median of the KDEs for mocks is shown in blue.

finally merged into voids (Douglass et al. 2023). Since VoidFinder does not compute voids with an effective radius larger than  $30 h^{-1}$  Mpc (Douglass et al. 2023) and PH computes many larger voids, we only compute  $V^2$  voids in the adopted KIAS-VAGC in this study for comparison with the computed PH voids.

We compute  $V^2$  voids using VAST toolbox (Douglass et al. 2022) with settings  $H_0 = 100 h \text{ km s}^{-1} \text{ Mpc}^{-1}$  and  $\Omega_m = 0.3$ . A total of 419 voids are reported with effective radius at least  $10 h^{-1}$  Mpc. We consider voids with  $R_{\text{eff}}$  at least  $20 h^{-1}$  Mpc, resulting in 150 voids. Figure 6A shows spherical approximations of PH voids and  $V^2$  voids based on  $R_{\text{eff}}$ . The zoomed-in panel on the right in the figure shows a PH void that is not found by  $V^2$ .

We first compare the number of topologically significant voids. We say that a PH void is topologically significant if the smallest hyperrectangle around its representative boundary contains at least one significant feature. For a  $V^2$  void, we compute the number of significant features in the smallest hyperrectangle around the sphere of the void’s effective radius centered at its centroid. For a fair comparison, we do the same for every PH void, and these are labeled as ‘spherical approximation’. Figure 6B shows that only 11 out of the 150  $V^2$  voids (green points) are topologically significant. On the other hand, all of the PH voids are topologically significant (blue points). Only around half of

the spherical approximations of PH voids do not contain a significant feature. However, they are still more than the number of topologically significant  $V^2$  voids. We further note that the discrepancy between the number of significant PH voids and significant spherical approximations of PH voids indicates that some of the PH voids are aspherical. Finally, we compare  $g(r)$  profiles for PH and  $V^2$  voids in the SDSS and mocks in Figure 6C. We note that the peak of  $g(r)$  for PH voids occurs at  $r < R_{\text{eff}}$  (at  $\frac{r}{R_{\text{eff}}} = 0.95$ ) whereas for  $V^2$  voids it occurs at  $r > R_{\text{eff}}$  (at  $\frac{r}{R_{\text{eff}}} = 1.15$ ). This indicates that voids inferred using the two different methodologies possess different morphologies.

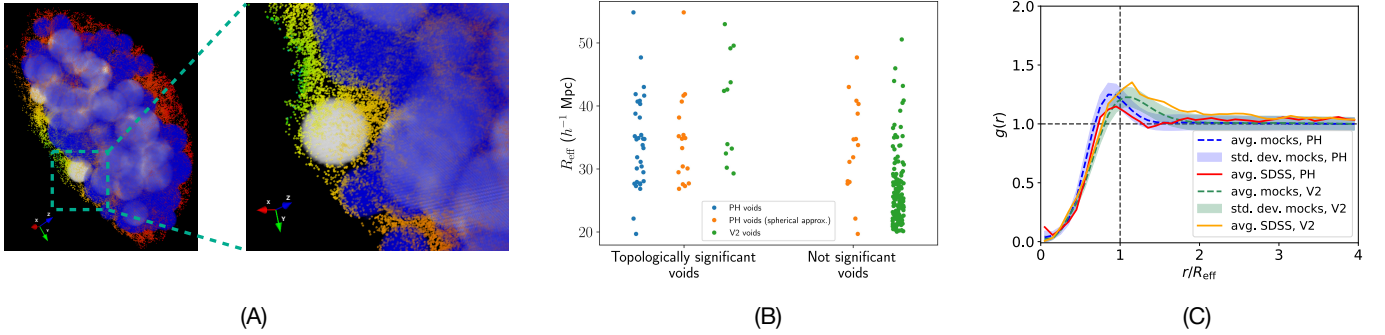


**Figure 6.** Comparing PH and  $V^2$  voids. (A) PH voids in white and  $V^2$  voids in blue. PH finds a void not found by  $V^2$ . (B) Distributions of  $R_{\text{eff}}$  of  $V^2$  and PH voids, categorized on the basis of whether their representative boundaries contain topologically significant features. Majority of  $V^2$  voids do not contain topologically significant features. (C)  $g(r)$  of PH and  $V^2$  for SDSS and mocks.

## 5. DISCUSSION

We have introduced a void finding algorithm that is based on the rigorous mathematics of persistent homology, and applied it to the SDSS DR7 main galaxy sample and a set of mock catalogs constructed from a cosmological scale dark matter simulation. Certain user inputs are required to define voids, and in this work a birth threshold of  $\tau_u = 22.5 h^{-1} \text{Mpc}$  and persistence level  $p = 7.5 h^{-1} \text{Mpc}$  are used to select topological robust objects from the galaxy point distribution. We find representative boundaries around 32 unique voids that satisfy the criteria imposed, comprising a total volume fraction of 0.26 of the SDSS footprint over the redshift range  $0.02 \leq z \leq 0.116$ . The physical properties of the voids have been ascertained; chiefly their radial profiles, effective radii distributions, the nearest neighbor separation, two-point correlation function and sphericity. We find a range of sizes between  $21 - 56 h^{-1} \text{Mpc}$ , and a median nearest neighbor separation of  $\sim 57 h^{-1} \text{Mpc}$ . The properties of these objects will depend on the choice of birth threshold and persistence. The SDSS voids show excellent agreement with the same quantities extracted from the mock catalogs, indicating that the large scale distribution of matter in the observed Universe closely match our expectations from simple cold dark matter gravitational physics. This is a non-trivial result – the mock galaxies have been selected to match the two point statistics of the SDSS, but the spatial distribution and morphological properties of voids carry information beyond the power spectrum. The void profiles;  $g(r)$ , obtained using persistent homology and the  $V^2$  algorithm are in reasonable agreement, indicating that the void profile is a robust statistical quantity that can be used for cosmological parameter estimation. However, the peak of  $g(r)$  occurs at mildly different  $r$  values for the two algorithms, indicating that the non-spherical nature of the voids will play some role in determining the average shape.

The topological objects defined in this work are constructed from the observed point distribution rather than a smoothed density field inferred from the galaxy positions. This makes it difficult to analytically relate the void properties to cosmological parameters, since the standard cosmological model is predicated on a fluid description of matter. However, there are a number of interesting avenues that remain to be explored. First, the sensitivity of the void properties to galaxy bias, and cosmological parameters, can be tested by applying our algorithm to other mock galaxy and dark matter data. We expect only mild dependence on galaxy bias, since all galaxies should trace the same wall-like structures on large scales. The cosmological parameters  $\Omega_m h^2$  and  $n_s$  will determine the extent to which the dark matter field fluctuates, and the void statistics may be sensitive to these quantities. Relating the topology of the point distribution to that of the smoothed density field is also an on-going point of interest. Persistence provides a way of divining the significance of features found using persistent homology. Alternatively, the smoothing scale used to

convert a point distribution into a continuous field washes out small scale holes and provides a measure of significance based on physical scale. In addition, smoothing with a Gaussian kernel will sphericalize voids that are roughly equal in size to the smoothing volume, an effect that will not be present in the voids inferred from the point distribution. The fluid and particle descriptions will only match on large scales, for objects significantly above the smoothing scale used to define the fluid. Relating the properties of voids obtained using the fluid and particle descriptions of matter would provide a link between the two different interpretations of the density field that generates spacetime curvature.

The topology of cosmological fields; the late time galaxy distribution, Cosmic Microwave Background, weak lensing maps, contains information beyond summary statistics that are commonly used by the community. Extracting this information, and comparing the results to mock data, provides an important consistency check of the  $\Lambda$ CDM model. Going further and inferring the ensemble average of topological summary statistics of random fields remains a long-standing goal.

## ACKNOWLEDGEMENTS

We warmly thank Juhan Kim and Sungwook E. Hong for generating the Horizon Run 4 mock galaxy catalogue used in this work. MT and SA are supported by an appointment to the JRG Program at the APCTP through the Science and Technology Promotion Fund and Lottery Fund of the Korean Government, and were also supported by the Korean Local Governments in Gyeongsangbuk-do Province and Pohang City. SA also acknowledges support from the NRF of Korea (Grant No. NRF-2022R1F1A1061590) funded by the Korean Government (MSIT). MT was supported by the National Research Foundation of Korea (NRF) grant funded by the Korea government (MSIT) (2022R1F1A1064313). We thank the Korea Institute for Advanced Study for providing computing resources (KIAS Center for Advanced Computation Linux Cluster System). A large data transfer was supported by KREONET, which is managed and operated by KISTI.

## APPENDIX

### A. PERSISTENT HOMOLOGY BACKGROUND AND TERMINOLOGY

Figure 7A shows an example of a discrete set of points or a point-cloud. It has many gaps and holes, but one stands out as a larger hole compared to others. Dimension-1 persistent homology (PH) computes the birth and death of holes across different spatial scales. This information is plotted as a persistence diagram (PD). Figure 7B shows dimension-1 PD computed for the example in Figure 7A. The persistence of a hole is defined as the difference between its death and birth. Those with higher persistence are more robust to noise in the data set. There is one feature (marked in red) with relatively higher dimension-1 persistence, as expected. Figure 7C shows multiple possible representative boundaries computed around the feature with maximum persistence.

### B. PH COMPUTATION

Locations of topological voids were determined by computing tight representative boundaries of significant  $H_2$  features in VR-filtration of the raw data. Features born at a spatial scale at most  $\tau_u$  and with persistence at least  $p$  were defined as significant. These parameters are user-defined. PH was computed up to threshold of  $\tau_u + p$  using Dory (Aggarwal & Periwai 2024), which implements the matrix reduction algorithm to compute PH (Carlsson & Zomorodian 2005). Matrices in Dory are represented using compressed sparse row format and the number of non-zero entries that can be represented is the upper limit of unsigned 32-bit int,  $l = 4294967295$ . However, computing PH for the galaxy data sets in this work resulted in matrices with more than  $l$  non-zero entries. Additionally, the number of non-zero columns also exceeds  $l$  in these computations. Both these issues were resolved by using a new sparse matrix format that increased the limits on numbers of non-zero elements in a matrix and non-zero columns to  $l^2$ .

### C. COMPUTING TIGHT REPRESENTATIVE BOUNDARIES

Representative boundaries for all topological features were computed and shortened using algorithms introduced in Aggarwal & Periwai (2023). Briefly, columns of the matrix of reduction operations are used as the initial set of representatives. Representative with birth parameters less than the user-defined birth threshold are greedily shortened by summing (modulus 2) boundaries pairwise that result in maximal reduction in lengths.

We now explain why the number of computed tight representatives can be less than the number of significant features. Figure 8A shows a simulated data set in two dimensions with three holes that visually stand out. The  $H_1$

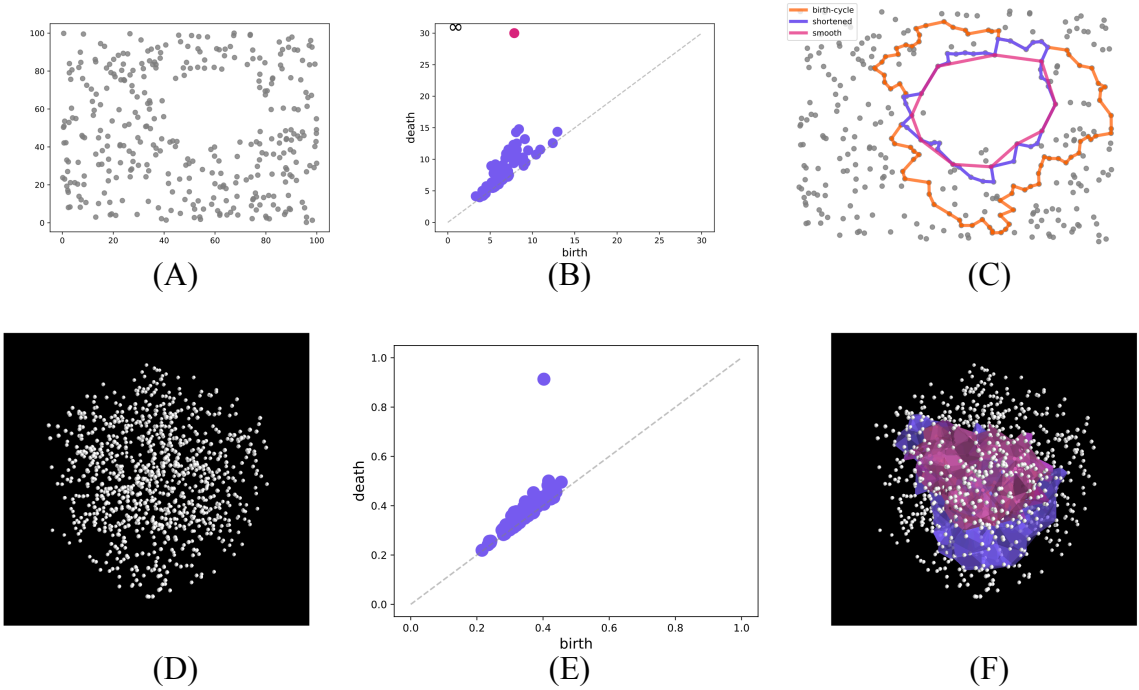


**Figure 7.** (A) A noisy discrete data set in with one significant hole. (B) The births and death of holes are plotted as a persistence diagram. This example shows that only one hole has relatively high persistence. (C) Representative boundaries tighten as they are shortened by our algorithm. (D) A point-cloud in 3D. No significant hole is visible. (E) PD shows that one feature has relatively high persistence. (F) Our algorithms improve geometric precision. The blue boundary is the birth-cycle from the recursive algorithm. The red boundary is the smooth cycle after applying the greedy shortening and smoothing algorithms.

PD in Figure 8B shows that there are three features with relatively high persistence. Figure 8C shows representative boundaries computed by the matrix reduction algorithm (black curves) around these features. The birth parameters of these features are 5.06, 4.98 and, 4.41. Geometrically, the birth parameter of a feature implies that the algorithm finds a cycle around the feature with the length of its longest edge equal to the birth parameter. Here we compute tight representatives with birth threshold  $\tau_u = 10$ . Representatives with birth parameters less than 10 are summed modulus 2 for greedy shortening. This process results in new representatives that may have the same or larger birth parameters, but smaller than  $\tau_u = 10$ . Figure 8C shows the representatives after greedy shortening in red. They are geometrically tighter around the features, however, their birth parameters are 8.23, 5.56, and, 9.2, all larger than the birth parameters of these features from the matrix reduction algorithm (5.06, 4.98 and, 4.41, respectively). The death parameter remains unchanged. As a result, death – birth of tight representatives might be less than the death – birth of the corresponding features that are computed by the matrix reduction algorithm. Consequently, the persistence of some of the tight representatives around significant features may be below the persistence threshold, classifying them as non-significant. Same reasoning follows for features of higher dimensions.

After greedy shortening, tight representatives that can potentially contain topologically significant features are stochastically shortened as follows. A local cover of the representative boundary is computed as the smallest hyper-rectangle with points of the boundary inside or on it. Stochasticity in the cover is introduced by perturbations and permutations as follows. First,  $n_{\text{pert}}$  perturbations (user-defined parameter) are constructed. The maximum perturbation parameter is initialized as  $\Delta_m = p/3$ . For each point  $p_i$ , we denote the distance of its nearest neighbor by  $d_i$ . Each point  $p_i$  is perturbed randomly in a neighborhood of radius  $r_i = \min\{d_i/3, \Delta_m\}$ .  $n_{\text{pert}}$  perturbations are constructed and PH upto  $\tau = \tau_u + p$  is computed for each perturbation. If the number of significant features in each of the  $n_{\text{pert}}$  perturbations is not the same as the number of significant features in the unperturbed cover, we halve  $\Delta_m$  and repeat. Otherwise, we are done with constructing perturbations of the cover. For each perturbation of a cover, we create  $n_{\text{perm}}$  permutations (user-defined parameter) as follows. A list of edges of lengths up to  $\tau$  is constructed that is sorted by their lengths. The lengths are rounded to decimal precision  $r$  (user-defined parameter). The order

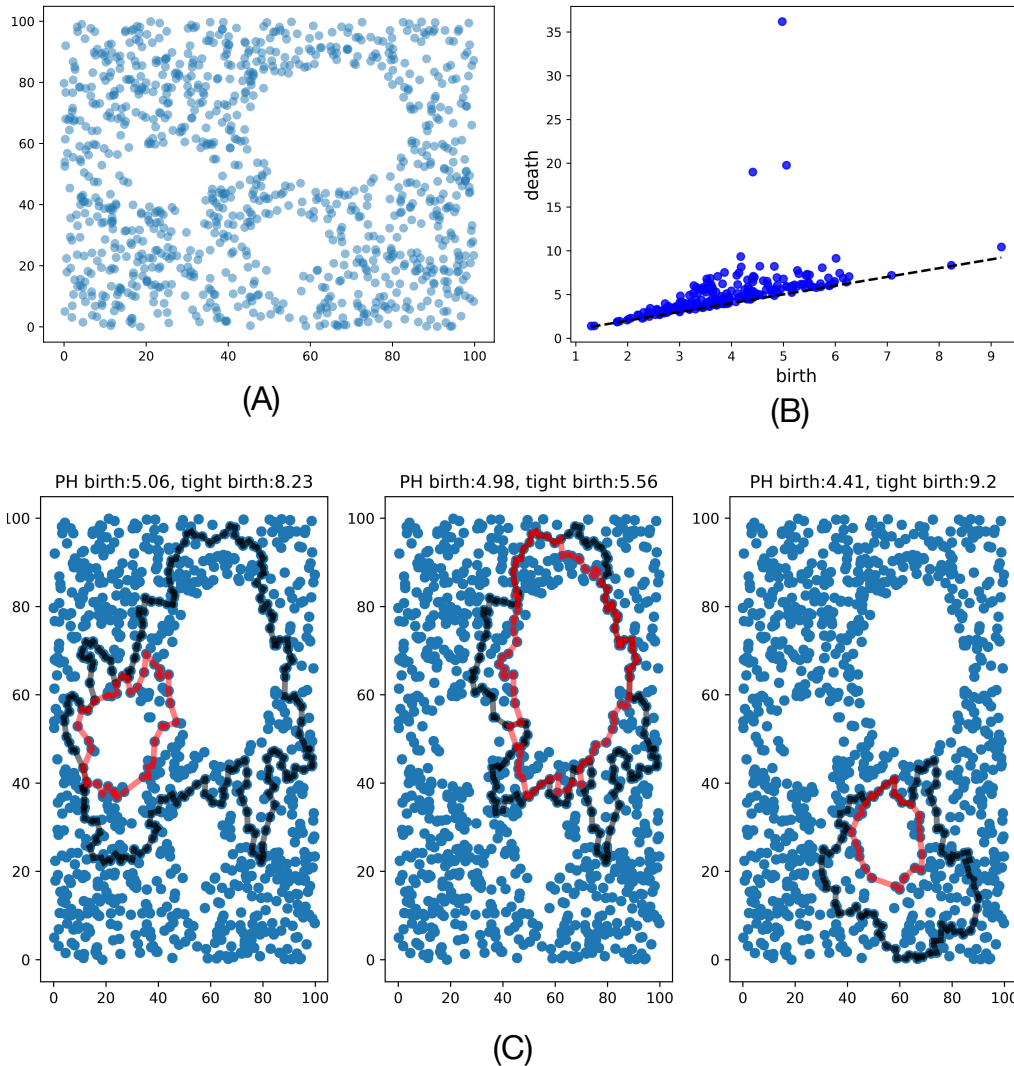


**Figure 8.** Number of tight representatives can be smaller than the number of significant features. (A) A simulated data set embedded in  $\mathbb{R}^2$  with three distinct holes. (B)  $H_1$  PD shows there are three features with relative high persistence. (C) Representatives from the matrix reduction algorithm are shown in black. Their birth parameters are 5.06, 4.98 and, 4.41. Tight representatives after greedy shortening ( $\tau_u = 10$ ) are shown in red. Their birth parameters are 8.23, 5.56, and, 9.2. Consequently, they have lower persistence and some may be classified as non-significant depending upon the persistence threshold.

of the sorted edges define the order of columns in the boundary and co-boundary matrices for PH and representative boundary computation. Permutations are constructed by permuting the order of edges of the same length. Note that the number of possible unique permutations might be less than  $n_{\text{perm}}$ . PH is computed for (at most)  $n_{\text{pert}} \times n_{\text{perm}}$  sorted lists of edges, for each cover, up to  $\tau$ . Representative boundaries born at a spatial scale at most  $\tau_u$  are also computed. From all computations for a cover, a set of all boundaries that possibly wrap around significant feature(s) is determined. Minimal boundaries are selected from these sets, and they are smoothed using algorithm detailed in S1 Text of [Aggarwal & Periwai \(2023\)](#).

#### D. CHOOSING PARAMETERS TO DEFINE SIGNIFICANT FEATURES

For all data sets in this work, we defined significant features as those born before  $\tau_u = 22.5 h^{-1}$  Mpc and with persistence at least  $p = 7.5 h^{-1}$  Mpc. Here, we explain these choices.

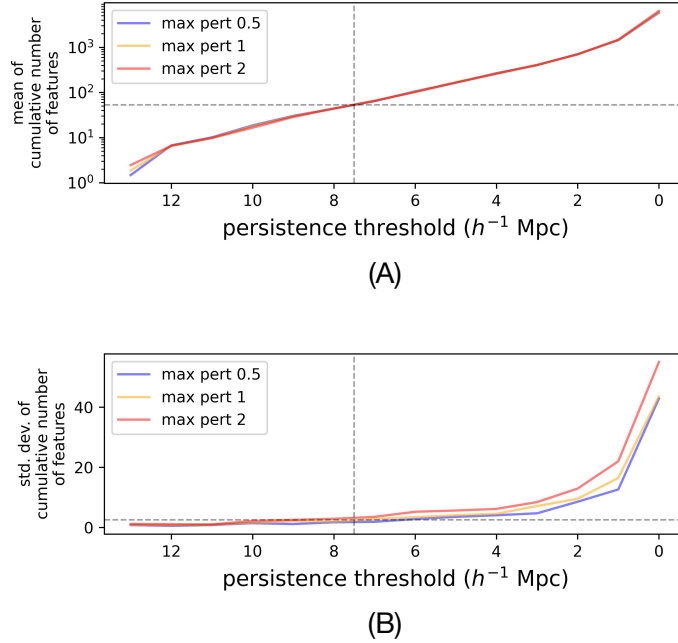


**Figure 9.** Number of  $H_2$  features is computed for 50 samples of three different perturbations of the data sets. Different colors show different magnitudes of the perturbation. (A) The mean number of features with persistence at most  $x$  decreases exponentially as  $x$  increases. (B) The standard deviation in the number of features is small and consistent across the three perturbations for persistence thresholds greater than  $7.5 h^{-1}$  Mpc (dashed vertical line).

#### D.1. Persistence threshold

First, we decide the value of persistence threshold. A higher persistence implies higher robustness to noise or perturbations in the data set. Hence, we perturbed location of each galaxy randomly in a ball of radius  $\Delta$  and computed PH. This was done for 50 samples for each of  $\Delta = \{0.5, 1, 2\} h^{-1}$  Mpc. Then, we count the number of  $H_2$  features. Figure 9A shows the mean of cumulative counts of features for the different values of  $\Delta$ . For instance, a point  $(x_*, y_*)$  on this curve informs that there are  $y_*$  non-trivial  $H_2$  features (averaged over the 50 samples) with persistence at most  $x_*$ . In other words, the  $x$ -axis is the persistence threshold. As expected, the number of features increases as persistence threshold decreases (notice that the  $x$  axis is reversed in the plot). Figure 9B shows the standard deviation in the cumulative number of features. In concordance with the implication of higher persistence, the standard deviation is lower at a higher persistence threshold. Moreover, at low persistence thresholds, standard deviations are inconsistent across the different values of  $\Delta$ . At  $x = 7.5$ , the standard deviation is small and consistent across the different perturbations. At higher thresholds, the number of features decreases exponentially (see Figure 9A). Hence, we choose  $p = 7.5 h^{-1}$  Mpc as a conservative choice for persistence threshold.

#### D.2. Birth threshold

Given a persistence threshold, we now decide the birth threshold. Figure 10A shows distribution of lengths of representatives, before and after greedy shortening, for different values of birth thresholds. We note that for birth thresholds greater than  $22.5 h^{-1}$  Mpc, the distributions of cycle lengths after greedy shortening are similar. Further, we compute the number of significant features at each birth threshold. Figure 10B shows that the peak in the number of significant features that are enclosed within a shortened representative is at  $22.5 h^{-1}$  Mpc. Hence, we choose  $\tau_u = 22.5 h^{-1}$  Mpc as the birth threshold to define significant features.

### E. SENSITIVITY OF VOID PROPERTIES TO DATA VARIATIONS

In this section we address two issues. First, we trim a small number of protruding surfaces in the angular footprint of the SDSS. Topological statistics are often particularly sensitive to complicated data boundaries, because the underlying point distribution is inhomogeneously sampled in these regions. Or in the language of smoothed fields, the underlying density field is subject to a larger noise component in the absence of data that is cut by the survey boundaries. We test that the voids found in this work are not significantly compromised by the boundary, by generating a slightly

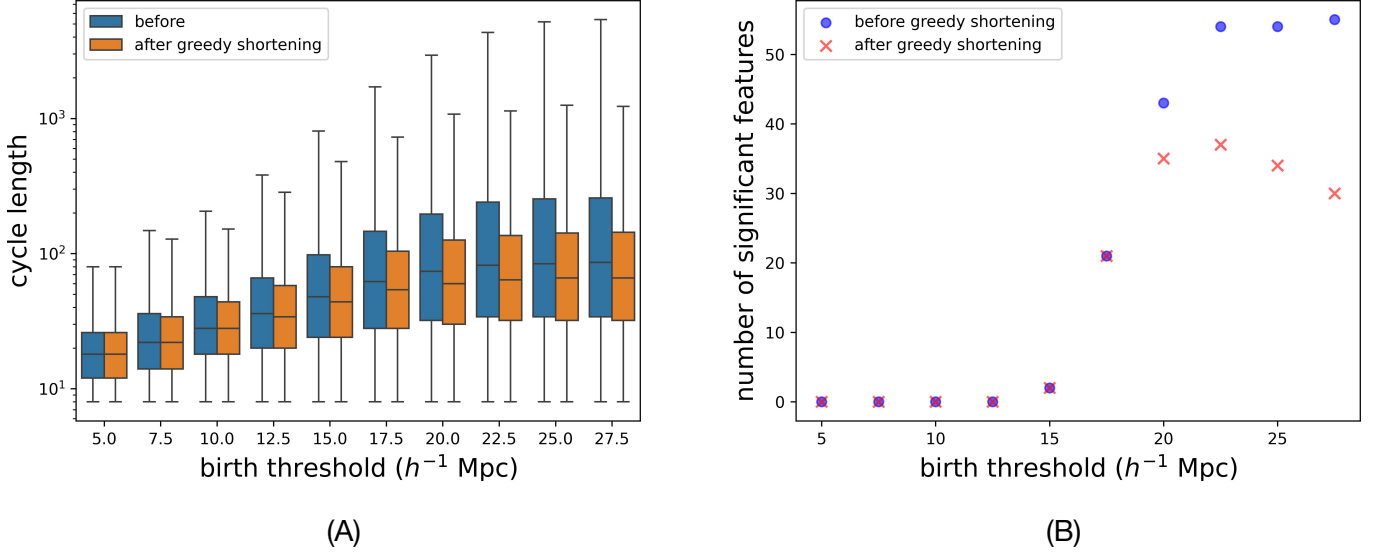


**Figure 10.** (A) Distributions of cycle lengths before and after greedy shortening at different birth thresholds ( $\tau_u$ ). The distributions are similar for  $\tau_u > 17.5 h^{-1}$  Mpc. (B) Number of significant features around which we can find a representative after greedy shortening attains maximum at  $\tau_u = 22.5 h^{-1}$  Mpc.

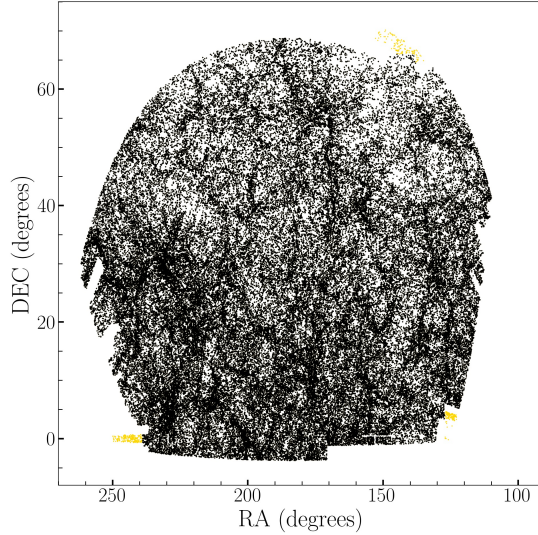


**Figure 11.** The angular distribution of SDSS galaxies on the sky. In the Appendix, we cut the gold points from the sample and re-analyze the data, to test the sensitivity of the void properties to the boundary.

simpler angular footprint. In Figure 11 we present the full data used in the main body of the paper, but the gold points are cut in this section. In what follows we call the new data set ‘trimmed’ (cf. black points, Figure 11) and the non-trimmed ‘original’. These particular regions were chosen to maximize the volume to surface area of the data and make the footprint closer to a spherical cap on the sky. If the data is bounded by a complicated mask geometry, then spurious triangulated meshes can be generated that cross the masked regions.

Second, we analyze robustness of the voids found by undersampling both original and trimmed data sets. We compute and compare PH and tight representatives of original and trimmed data sets that are undersampled at three different sampling percentages of  $p = 95, 90$  and,  $80\%$  (three samples each). We call original and trimmed data sets as catalogs. Then, comparison of catalog1-catalog2 at percentages  $p_1$ - $p_2$  is the Mann-Whitney U rank test of distributions of centroids of a sample of catalog1 at percentage  $p_1$  with that of a sample of catalog2 at percentage  $p_2$ . This is done for

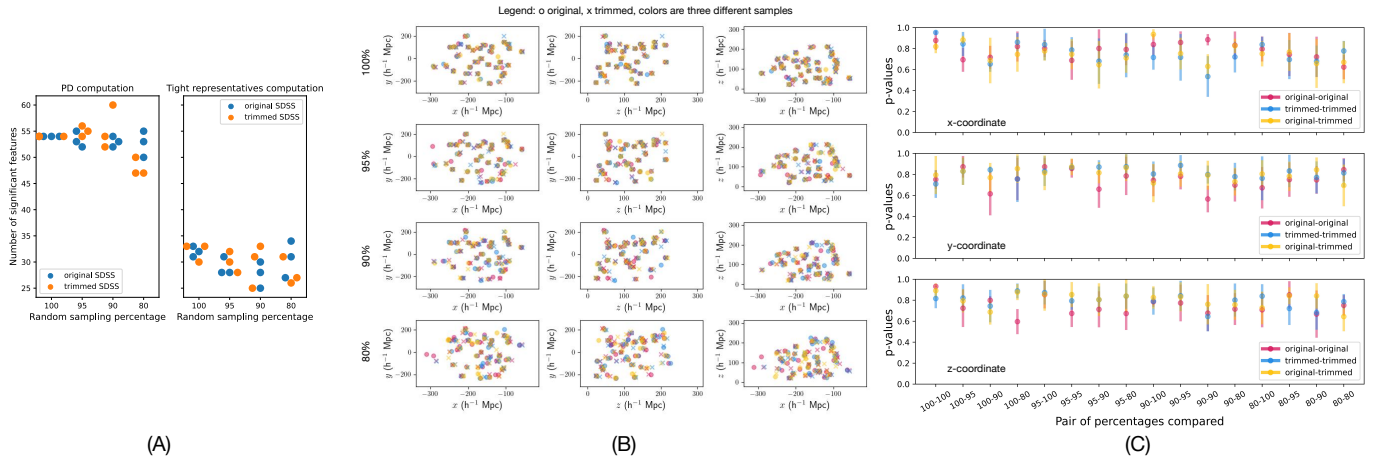


**Figure 12.** Comparing PH and tight representatives of different samples of original and trimmed data sets at different sampling percentages. (A) Number of significant features in PD and number of tight representatives computed when birth and persistence thresholds were kept the same across all samples ( $\tau_u = 22.5 h^{-1}$  Mpc,  $\epsilon = 7.5 h^{-1}$  Mpc). (B) Centroids of computed voids. (C) Results of the Mann-Whitney U rank test for comparing distributions of  $x$ ,  $y$  and,  $z$  coordinates of void centroids for all pairwise combinations show that these distributions cannot be statistically distinguished ( $p$ -values  $\gg 0.05$ ).

all pairwise combinations of samples (6 combinations if catalog1 = catalog2, and 9 combinations otherwise), resulting in a distribution of  $p$ -values of statistical significance.

We also compare computations for three samples of full data sets (100%) such that the order of edges of same lengths in the matrix reduction algorithm are shuffled. Such a shuffling will have no effect on the persistence diagram, but the computed tight representatives might be different. These samples are shown as 100% shuffling in the figures. The birth and persistence thresholds for all data sets are  $\tau_u = 22.5 h^{-1}$  Mpc and  $\epsilon = 7.5 h^{-1}$  Mpc, respectively.

Figure 12A shows the number of significant features from PD computation and the number of computed tight representatives. The number of significant features from PD computation in the full original and trimmed data sets are exactly the same, as expected. The number of computed tight representatives varies between 30 and 33 for the different shuffled full data sets of original and trimmed. The variance in the number of significant features and number of tight representatives increases at percentages 90 and 80.

We next compare the centroids of the computed tight representatives. Figure 12(B) shows coordinates of the centroids for all cases—original is shown by o marker, trimmed by x marker, and different colors show the different samples. We note that majority of o and x match and the pattern is also similar as sampling percentage decreases (comparing top to bottom). We quantify this by conducting Mann-Whitney U rank test for  $x$ ,  $y$ , and  $z$  coordinates. Figure 12(C) shows that the  $p$ -values from this significance test are  $\gg 0.05$ , indicating that these distributions cannot be statistically distinguished.

## F. INFORMATION FOR VOID CENTROIDS

Table 1 shows centroids,  $R_{\text{eff}}$ , and sphericity of the tight representatives computed for PH voids in SDSS. The three different samples (Sample 0, 1, and 2) correspond to tight representatives computed for three different bijective mappings of galaxies to integers. Such permutations will not affect the persistence diagrams but can result in differences in the tight representative computation due to the stochasticity of our algorithm. Nevertheless, Figure 12C shows that these differences are not significant— $p$ -values for 100-100 comparison for both original and trimmed are much greater than 0.05 and very close to 1. The main text uses results of Sample 1.

## G. SUPPLEMENTARY INFORMATION

### G.1. Computation cost

Figure 13 shows computation costs for the different steps of computing tight representatives (up to spatial scale of  $30 h^{-1}$  Mpc and greedy shortening).

## REFERENCES



**Table 1.** SDSS void centroids of the computed tight representatives

Sample 0					Sample 1					Sample 2				
ra	dec	z	$R_{\text{eff}}$	$\psi$	ra	dec	z	$R_{\text{eff}}$	$\psi$	ra	dec	z	$R_{\text{eff}}$	$\psi$
236.62	26.3	0.101	43.62	0.78	235.8	25.63	0.1013	41.63	0.78	236.44	26.35	0.1008	44.04	0.74
172.34	33.83	0.0941	51.86	0.75	172.31	34.23	0.0941	54.84	0.73	174.59	34.82	0.0938	46.64	0.77
125.57	44.47	0.0872	44.05	0.8	211.55	43.61	0.0539	47.69	0.77	125.64	46.12	0.0885	42.87	0.8
196.07	21.55	0.0975	48.33	0.75	125.14	44.77	0.0879	41.86	0.78	155.34	21.14	0.0926	43.15	0.77
224.22	4.4	0.1048	33.8	0.8	217.43	9.46	0.0752	40.69	0.76	213.5	43.31	0.0522	46.3	0.74
210.25	43.62	0.0519	45.78	0.77	223.64	3.97	0.1051	34.89	0.78	217.26	9.45	0.0757	40.77	0.74
216.85	10.13	0.0754	39.14	0.74	193.08	22.35	0.0977	43.0	0.8	224.47	4.25	0.1035	33.52	0.84
154.99	22.23	0.0965	43.53	0.75	213.6	30.73	0.0953	40.3	0.81	193.14	21.55	0.0975	44.04	0.81
134.56	46.17	0.0622	36.01	0.8	156.97	21.87	0.0947	40.82	0.78	213.39	30.56	0.0972	41.9	0.8
212.36	29.64	0.0981	41.9	0.82	201.06	20.25	0.0565	34.75	0.8	134.12	45.49	0.062	35.97	0.8
149.28	12.51	0.0911	39.62	0.78	133.31	45.48	0.0608	35.39	0.79	157.98	19.34	0.0732	32.58	0.81
157.14	29.53	0.1061	33.64	0.85	148.39	13.01	0.0916	38.77	0.82	157.26	28.93	0.1057	33.84	0.83
199.41	19.34	0.0544	35.75	0.8	239.96	12.7	0.0823	34.68	0.83	199.66	19.4	0.0555	34.17	0.79
157.37	18.15	0.0732	35.9	0.81	142.68	17.49	0.0618	35.19	0.83	143.46	17.33	0.0607	33.89	0.82
155.57	30.59	0.0604	38.61	0.79	157.08	29.31	0.1058	33.3	0.86	233.75	13.08	0.0652	34.23	0.83
142.42	17.74	0.062	35.29	0.79	155.28	33.37	0.0628	38.15	0.77	179.27	28.27	0.0644	27.86	0.81
152.01	38.67	0.0992	28.13	0.86	152.84	38.95	0.0996	29.47	0.79	152.83	30.89	0.0607	36.6	0.81
126.78	42.1	0.0728	29.74	0.83	179.29	29.21	0.0634	27.57	0.84	169.64	38.13	0.0532	30.92	0.83
234.06	13.46	0.067	29.46	0.86	126.73	41.27	0.0725	30.39	0.83	152.83	38.78	0.0972	27.37	0.86
177.87	28.67	0.0642	27.26	0.83	233.83	10.2	0.0641	27.92	0.85	135.28	9.31	0.0999	30.76	0.8
194.05	14.33	0.1058	32.79	0.82	232.06	44.66	0.0828	31.85	0.81	195.01	60.23	0.0844	33.1	0.88
192.74	60.28	0.0826	33.17	0.86	192.45	60.6	0.0847	34.79	0.84	214.6	12.66	0.0501	30.53	0.85
189.11	35.92	0.0751	31.07	0.82	193.04	14.69	0.1061	33.78	0.82	193.07	14.78	0.1062	35.24	0.82
217.38	10.37	0.0466	30.04	0.83	211.92	11.65	0.052	28.05	0.85	231.51	44.58	0.0837	31.65	0.86
201.79	27.99	0.0811	26.85	0.84	134.48	10.15	0.0996	31.12	0.79	126.12	41.95	0.0735	28.08	0.87
230.87	45.3	0.0838	30.41	0.88	200.33	28.02	0.0822	27.7	0.87	189.06	37.16	0.0773	28.06	0.85
136.2	8.66	0.1004	28.79	0.82	227.21	25.87	0.0936	30.07	0.78	201.51	28.02	0.0812	26.9	0.81
132.45	31.73	0.0345	27.31	0.89	189.94	37.18	0.0779	26.84	0.87	227.76	24.92	0.096	28.03	0.81
151.46	36.82	0.0858	25.5	0.91	151.04	38.06	0.0841	27.28	0.89	150.8	37.11	0.0852	26.49	0.88
141.57	47.16	0.0992	18.82	0.94	132.26	30.77	0.0341	27.66	0.88	127.11	27.94	0.0613	26.51	0.81
205.06	24.72	0.1	22.88	0.9	206.11	25.47	0.0987	22.12	0.91	133.42	32.51	0.0353	26.87	0.92
-	-	-	-	-	142.38	46.01	0.0993	19.68	0.92	205.26	24.53	0.0991	25.44	0.91
-	-	-	-	-	-	-	-	-	-	141.95	45.46	0.0995	20.05	0.91

—. 2024, *Journal of Computational Science*, 79, 102290

Aragon-Calvo, M. A., van de Weygaert, R., Araya-Melo, P., Platen, E., & Szalay, A. S. 2010, *Mon. Not. Roy. Astron. Soc.*, 404, 89, doi: [10.1111/j.1745-3933.2010.00841.x](https://doi.org/10.1111/j.1745-3933.2010.00841.x)

Baldauf, T., Codis, S., Desjacques, V., & Pichon, C. 2016, *Monthly Notices of the Royal Astronomical Society*, 456, 3985, doi: [10.1093/mnras/stv2973](https://doi.org/10.1093/mnras/stv2973)

Bardeen, J. M., Bond, J. R., Kaiser, N., & Szalay, A. S. 1986, *ApJ*, 304, 15, doi: [10.1086/164143](https://doi.org/10.1086/164143)

Bendich, P., Marron, J. S., Miller, E., Pieloch, A., & Skwerer, S. 2016, *The annals of applied statistics*, 10, 198

Blanton, M. R., Schlegel, D. J., Strauss, M. A., et al. 2005, *AJ*, 129, 2562, doi: [10.1086/429803](https://doi.org/10.1086/429803)

Bond, J. R., Kofman, L., & Pogosyan, D. 1996, *Nature*, 380, 603, doi: [10.1038/380603a0](https://doi.org/10.1038/380603a0)

Bos, E. G. P., van de Weygaert, R., Dolag, K., & Pettorino, V. 2012, *Mon. Not. Roy. Astron. Soc.*, 426, 440, doi: [10.1111/j.1365-2966.2012.21478.x](https://doi.org/10.1111/j.1365-2966.2012.21478.x)

Brüel-Gabrielsson, R., Ganapathi-Subramanian, V., Skraba, P., & Guibas, L. J. 2018, arXiv e-prints, arXiv:1811.12543, doi: [10.48550/arXiv.1811.12543](https://doi.org/10.48550/arXiv.1811.12543)

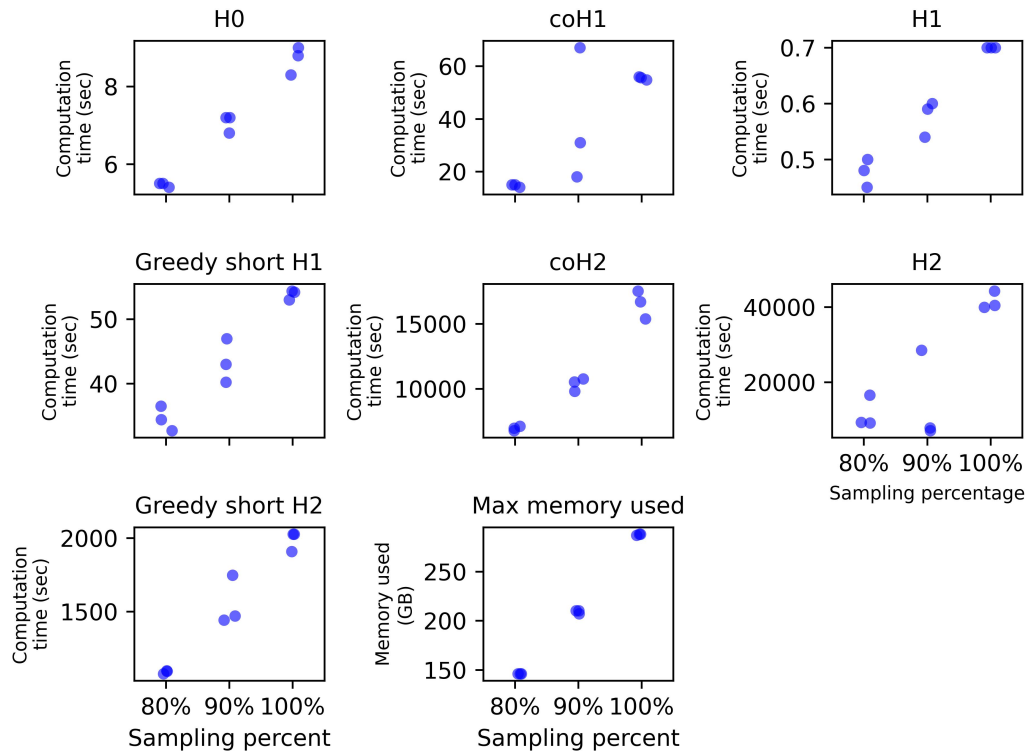


**Figure 13.** Computation times and memory for different under samples of the SDSS data set.

- Cai, Y.-C., Padilla, N., & Li, B. 2015, *Monthly Notices of the Royal Astronomical Society*, 451, 1036, doi: [10.1093/mnras/stv777](https://doi.org/10.1093/mnras/stv777)
- Carlsson, G. 2009, *Bulletin of the American Mathematical Society*, 46, 255
- Carlsson, G., & Zomorodian, A. 2005, *Discrete Comput. Geom.*, 33, 249
- Chan, K. C., Hamaus, N., & Biagetti, M. 2019, *Phys. Rev. D*, 99, 121304, doi: [10.1103/PhysRevD.99.121304](https://doi.org/10.1103/PhysRevD.99.121304)
- Choi, Y.-Y., Han, D.-H., & Kim, S.-S. S. 2010, *Journal of Korean Astronomical Society*, 43, 191, doi: [10.5303/JKAS.2010.43.6.191](https://doi.org/10.5303/JKAS.2010.43.6.191)
- Codis, S., Pogosyan, D., & Pichon, C. 2018, *Monthly Notices of the Royal Astronomical Society*, 479, 973, doi: [10.1093/mnras/sty1643](https://doi.org/10.1093/mnras/sty1643)
- Colberg, J. M., Krughoff, K. S., & Connolly, A. J. 2005, *MNRAS*, 359, 272, doi: [10.1111/j.1365-2966.2005.08897.x](https://doi.org/10.1111/j.1365-2966.2005.08897.x)
- Colless, M., Dalton, G., Maddox, S., et al. 2001, *MNRAS*, 328, 1039, doi: [10.1046/j.1365-8711.2001.04902.x](https://doi.org/10.1046/j.1365-8711.2001.04902.x)
- Contarini, S., Pisani, A., Hamaus, N., et al. 2022a. <https://arxiv.org/abs/2212.03873>
- . 2022b. <https://arxiv.org/abs/2212.07438>
- de Vaucouleurs, G., de Vaucouleurs, A., Corwin, Herold G., J., et al. 1991, *Third Reference Catalogue of Bright Galaxies*
- Douglass, K. A., Veyrat, D., & BenZvi, S. 2023, *The Astrophysical Journal Supplement Series*, 265, 7
- Douglass, K. A., Veyrat, D., O’Neill, S. W., et al. 2022, *Journal of Open Source Software*, 7, 4033
- Dubinski, J., Kim, J., Park, C., & Humble, R. 2004, *NewA*, 9, 111, doi: [10.1016/j.newast.2003.08.002](https://doi.org/10.1016/j.newast.2003.08.002)
- Edelsbrunner, H., & Harer, J. L. 2022, *Computational topology: an introduction* (American Mathematical Society)
- El-Ad, H., & Piran, T. 1997, *The Astrophysical Journal*, 491, 421
- Falco, E. E., Kurtz, M. J., Geller, M. J., et al. 1999, *PASP*, 111, 438, doi: [10.1086/316343](https://doi.org/10.1086/316343)
- Feldbrugge, J., van Engelen, M., van de Weygaert, R., Pranav, P., & Vegter, G. 2019, *JCAP*, 09, 052, doi: [10.1088/1475-7516/2019/09/052](https://doi.org/10.1088/1475-7516/2019/09/052)
- Gott, J. Richard, I., Melott, A. L., & Dickinson, M. 1986, *ApJ*, 306, 341, doi: [10.1086/164347](https://doi.org/10.1086/164347)
- Gregory, S. A., & Thompson, L. A. 1978, *ApJ*, 222, 784, doi: [10.1086/156198](https://doi.org/10.1086/156198)
- Hamaus, N., Pisani, A., Choi, J.-A., et al. 2020, *JCAP*, 12, 023, doi: [10.1088/1475-7516/2020/12/023](https://doi.org/10.1088/1475-7516/2020/12/023)
- Hamaus, N., Sutter, P. M., Lavaux, G., & Wandelt, B. D. 2015, *JCAP*, 11, 036, doi: [10.1088/1475-7516/2015/11/036](https://doi.org/10.1088/1475-7516/2015/11/036)

- Hamaus, N., Wandelt, B. D., Sutter, P. M., Lavaux, G., & Warren, M. S. 2014, *Phys. Rev. Lett.*, 112, 041304, doi: [10.1103/PhysRevLett.112.041304](https://doi.org/10.1103/PhysRevLett.112.041304)
- Hong, S. E., Park, C., & Kim, J. 2016, *ApJ.*, 823, 103
- Icke, V., & Weygaert, R. 1987, *Astronomy and Astrophysics*, 184, 16
- Jennings, E., Li, Y., & Hu, W. 2013, *Monthly Notices of the Royal Astronomical Society*, 434, 2167, doi: [10.1093/mnras/stt1169](https://doi.org/10.1093/mnras/stt1169)
- Jiang, C. Y., Jing, Y. P., Faltenbacher, A., Lin, W. P., & Li, C. 2008, *ApJ.*, 675, 1095
- Jóeveer, M., Einasto, J., & Tago, E. 1978, *Monthly Notices of the Royal Astronomical Society*, 185, 357, doi: [10.1093/mnras/185.2.357](https://doi.org/10.1093/mnras/185.2.357)
- Kaiser, N. 1987, *MNRAS*, 227, 1, doi: [10.1093/mnras/227.1.1](https://doi.org/10.1093/mnras/227.1.1)
- Kerscher, M., Schmalzing, J., Buchert, T., & Wagner, H. 1998, *Astron. Astrophys.*, 333, 1, <https://arxiv.org/abs/astro-ph/9704028>
- Kim, J., Park, C., L’Huillier, B., & Hong, S. E. 2015, *JKAS*, 48, 213
- Klypin, A. A., & Shandarin, S. F. 1983, *Monthly Notices of the Royal Astronomical Society*, 204, 891, doi: [10.1093/mnras/204.3.891](https://doi.org/10.1093/mnras/204.3.891)
- Komatsu, E., Dunkley, J., Nolta, M. R., et al. 2009, *ApJS*, 180, 330, doi: [10.1088/0067-0049/180/2/330](https://doi.org/10.1088/0067-0049/180/2/330)
- Kovács, A., Vielzeuf, P., Ferrero, I., et al. 2022, *Monthly Notices of the Royal Astronomical Society*, 515, 4417, doi: [10.1093/mnras/stac2011](https://doi.org/10.1093/mnras/stac2011)
- Kramár, M., Goulet, A., Kondic, L., & Mischaikow, K. 2013, *Physical Review E*, 87, 042207
- Landy, S. D., & Szalay, A. S. 1993, *ApJ*, 412, 64, doi: [10.1086/172900](https://doi.org/10.1086/172900)
- Lavaux, G., & Wandelt, B. D. 2012, *The Astrophysical Journal*, 754, 109
- Lawson, P., Sholl, A. B., Brown, J., Fasy, B. T., & Wenk, C. 2019, *Scientific reports*, 9, 1
- Lee, J., & Park, D. 2009, *The Astrophysical Journal*, 696, L10, doi: [10.1088/0004-637X/696/1/L10](https://doi.org/10.1088/0004-637X/696/1/L10)
- Libeskind, N. I., et al. 2018, *Mon. Not. Roy. Astron. Soc.*, 473, 1195, doi: [10.1093/mnras/stx1976](https://doi.org/10.1093/mnras/stx1976)
- Lumsden, S. L., Heavens, A. F., & Peacock, J. A. 1989, *Monthly Notices of the Royal Astronomical Society*, 238, 293, doi: [10.1093/mnras/238.2.293](https://doi.org/10.1093/mnras/238.2.293)
- Massara, E., Villaescusa-Navarro, F., Viel, M., & Sutter, P. M. 2015, *JCAP*, 11, 018, doi: [10.1088/1475-7516/2015/11/018](https://doi.org/10.1088/1475-7516/2015/11/018)
- McGuirl, M. R., Volkening, A., & Sandstede, B. 2020, *Proceedings of the National Academy of Sciences*, 117, 5113
- Mecke, K. R., Buchert, T., & Wagner, H. 1994, *Astron. Astrophys.*, 288, 697, <https://arxiv.org/abs/astro-ph/9312028>
- Melott, A. L. 1990, *Physics Reports*, 193, 1, doi: [https://doi.org/10.1016/0370-1573\(90\)90162-U](https://doi.org/10.1016/0370-1573(90)90162-U)
- Nadathur, S., Woodfinden, A., Percival, W. J., et al. 2020, *Monthly Notices of the Royal Astronomical Society*, 499, 4140, doi: [10.1093/mnras/staa3074](https://doi.org/10.1093/mnras/staa3074)
- Neyrinck, M. C. 2008, *Monthly notices of the royal astronomical society*, 386, 2101
- Nicolau, M., Levine, A. J., & Carlsson, G. 2011, *Proceedings of the National Academy of Sciences*, 108, 7265
- Pan, D. C., Vogeley, M. S., Hoyle, F., Choi, Y.-Y., & Park, C. 2012, *Monthly Notices of the Royal Astronomical Society*, 421, 926
- Park, C., Pranav, P., Chingangbam, P., et al. 2013, *Journal of Korean Astronomical Society*, 46, doi: [10.5303/JKAS.2013.46.3.125](https://doi.org/10.5303/JKAS.2013.46.3.125)
- Park, C., Lee, J., Kim, J., et al. 2022, *The Astrophysical Journal*, 937, 15
- Platen, E., van de Weygaert, R., & Jones, B. J. T. 2007, *Mon. Not. Roy. Astron. Soc.*, 380, 551, doi: [10.1111/j.1365-2966.2007.12125.x](https://doi.org/10.1111/j.1365-2966.2007.12125.x)
- . 2008, *Mon. Not. Roy. Astron. Soc.*, 387, 128, doi: [10.1111/j.1365-2966.2008.13019.x](https://doi.org/10.1111/j.1365-2966.2008.13019.x)
- Pollina, G., et al. 2019, *Mon. Not. Roy. Astron. Soc.*, 487, 2836, doi: [10.1093/mnras/stz1470](https://doi.org/10.1093/mnras/stz1470)
- Pranav, P. 2021. <https://arxiv.org/abs/2109.08721>
- Pranav, P., van de Weygaert, R., Vegter, G., et al. 2019, *Mon. Not. Roy. Astron. Soc.*, 485, 4167, doi: [10.1093/mnras/stz541](https://doi.org/10.1093/mnras/stz541)
- Ryden, B. S. 1995, *ApJ*, 452, 25, doi: [10.1086/176277](https://doi.org/10.1086/176277)
- Saunders, W., Sutherland, W. J., Maddox, S. J., et al. 2000, *MNRAS*, 317, 55, doi: [10.1046/j.1365-8711.2000.03528.x](https://doi.org/10.1046/j.1365-8711.2000.03528.x)
- Schuster, N., Hamaus, N., Dolag, K., & Weller, J. 2023, *JCAP*, 05, 031, doi: [10.1088/1475-7516/2023/05/031](https://doi.org/10.1088/1475-7516/2023/05/031)
- Sheth, R. K., & van de Weygaert, R. 2004, *Mon. Not. Roy. Astron. Soc.*, 350, 517, doi: [10.1111/j.1365-2966.2004.07661.x](https://doi.org/10.1111/j.1365-2966.2004.07661.x)
- Shim, J., Codis, S., Pichon, C., Pogosyan, D., & Cadiou, C. 2021a, *Mon. Not. Roy. Astron. Soc.*, 502, 3885, doi: [10.1093/mnras/stab263](https://doi.org/10.1093/mnras/stab263)
- Shim, J., Park, C., Kim, J., & Hong, S. E. 2023, *Astrophys. J.*, 952, 59, doi: [10.3847/1538-4357/acd852](https://doi.org/10.3847/1538-4357/acd852)
- Shim, J., Park, C., Kim, J., & Hwang, H. S. 2021b, *Astrophys. J.*, 908, 211, doi: [10.3847/1538-4357/abd0f6](https://doi.org/10.3847/1538-4357/abd0f6)
- Sousbie, T., Pichon, C., & Kawahara, H. 2011, *Monthly Notices of the Royal Astronomical Society*, 414, 384, doi: [10.1111/j.1365-2966.2011.18395.x](https://doi.org/10.1111/j.1365-2966.2011.18395.x)

- Spolyar, D., Sahlén, M., & Silk, J. 2013, *Phys. Rev. Lett.*, 111, 241103, doi: [10.1103/PhysRevLett.111.241103](https://doi.org/10.1103/PhysRevLett.111.241103)
- Sutter, P., Lavaux, G., Hamaus, N., et al. 2015, *Astronomy and Computing*, 9, 1, doi: <https://doi.org/10.1016/j.ascom.2014.10.002>
- Sutter, P. M., Lavaux, G., Wandelt, B. D., & Weinberg, D. H. 2012, *Astrophys. J.*, 761, 187, doi: [10.1088/0004-637X/761/2/187](https://doi.org/10.1088/0004-637X/761/2/187)
- Sutter, P. M., Pisani, A., Wandelt, B. D., & Weinberg, D. H. 2014, *Mon. Not. Roy. Astron. Soc.*, 443, 2983, doi: [10.1093/mnras/stu1392](https://doi.org/10.1093/mnras/stu1392)
- Taylor, D., Klimm, F., Harrington, H. A., et al. 2015, *Nature communications*, 6, 1
- Tegmark, M., Blanton, M. R., Strauss, M. A., et al. 2004, *ApJ*, 606, 702, doi: [10.1086/382125](https://doi.org/10.1086/382125)
- Verza, G., Pisani, A., Carbone, C., Hamaus, N., & Guzzo, L. 2019, *JCAP*, 12, 040, doi: [10.1088/1475-7516/2019/12/040](https://doi.org/10.1088/1475-7516/2019/12/040)
- Vogeley, M. S., Geller, M. J., Park, C., & Huchra, J. P. 1994a, *AJ*, 108, 745, doi: [10.1086/117110](https://doi.org/10.1086/117110)
- Vogeley, M. S., Park, C., Geller, M. J., Huchra, J. P., & Gott, J. Richard, I. 1994b, *ApJ*, 420, 525, doi: [10.1086/173583](https://doi.org/10.1086/173583)
- Weygaert, R. v. d., & Bond, J. R. 2008, *Clusters and the Theory of the Cosmic Web*, ed. M. Plionis, D. Hughes, & O. López-Cruz (Dordrecht: Springer Netherlands), 335–408, doi: [10.1007/978-1-4020-6941-3\\_10](https://doi.org/10.1007/978-1-4020-6941-3_10)
- White, S. D. M., Frenk, C. S., Davis, M., & Efstathiou, G. 1987, *ApJ*, 313, 505, doi: [10.1086/164990](https://doi.org/10.1086/164990)
- Wilding, G., Nevenzeel, K., van de Weygaert, R., et al. 2021, *Mon. Not. Roy. Astron. Soc.*, 507, 2968, doi: [10.1093/mnras/stab2326](https://doi.org/10.1093/mnras/stab2326)
- Woodfinden, A., Nadathur, S., Percival, W. J., et al. 2022, *Mon. Not. Roy. Astron. Soc.*, 516, 4307, doi: [10.1093/mnras/stac2475](https://doi.org/10.1093/mnras/stac2475)
- Xu, X., Cisewski-Kehe, J., Green, S. B., & Nagai, D. 2019, *Astronomy and Computing*, 27, 34
- Zhu, X. 2013, in *IJCAI*, 1953–1959